

AD703295

DASA 2404  
AJA-R-6813-777

# SPHERICAL WAVES IN INELASTIC MATERIALS

J. Isenberg  
A. K. Bhaumik  
F. S. Weng

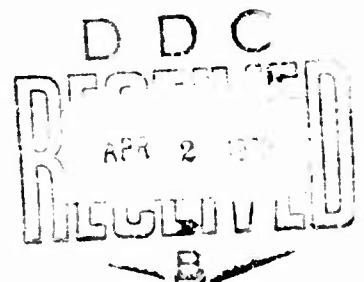
March 1970

Prepared for  
DEFENSE ATOMIC SUPPORT AGENCY  
Washington, D.C. 20305

AGBABIAN-JACOBSEN ASSOCIATES  
Los Angeles, California 90045

Contract No. DASA01-68-C-0081

Reproduced by the  
CLEARINGHOUSE  
for Federal Scientific & Technical  
Information Springfield Va 22151



AJA

R-6813-777

"This document has been approved for public release  
and sale; its distribution is unlimited."

ACCESSION FOR	
CFSTI	WHITE SECTION <input checked="" type="checkbox"/>
DOC	BUFF SECTION <input type="checkbox"/>
UNANNOUNCED	<input type="checkbox"/>
JUSTIFICATION	
DISTRIBUTION AVAILABILITY CODES	
DIST.	AVAIL. AND SPECIAL

**DASA 2404**  
**AJA-R-6813-777**

# **SPHERICAL WAVES IN INELASTIC MATERIALS**

**J. Isenberg  
A. K. Bhaumik  
F. S. Wong**

**March 1970**

**Prepared for**  
**DEFENSE ATOMIC SUPPORT AGENCY**  
**Washington, D.C. 20305**

**AGBABIAN-JACOBSEN ASSOCIATES**  
**Los Angeles, California 90045**

**Contract No. DASA01-68-C-0081**

**This work was sponsored by the  
Defense Atomic Support Agency Under NWER Subtask SB047**

## CONTENTS

<u>Section</u>		<u>Page</u>
1	INTRODUCTION . . . . .	1
2	FINITE ELEMENT METHOD . . . . .	3
3	MATHEMATICAL MODEL OF MATERIAL PROPERTIES . . . . .	7
4	PROPERTIES OF ROCK USED IN FINITE ELEMENT CALCULATIONS .	11
	Bulk Modulus . . . . .	11
	Shear Modulus . . . . .	13
	Yield Criteria . . . . .	13
	Density . . . . .	17
	Previous Work . . . . .	17
5	NUMERICAL RESULTS . . . . .	19
	Stress/Time Histories . . . . .	21
	Hoop Tensile Stress . . . . .	25
	$\sigma_r/\sigma_\theta$ Trajectories . . . . .	26
	Dilatancy and $\tau/\gamma$ . . . . .	28
	Growth of Cavity . . . . .	31
	Attenuation Rates . . . . .	32
	Effect of Pulse Shape on Wave Properties . . . . .	34
6	IMPLICATIONS FOR MATERIAL PROPERTY TESTING . . . . .	37
7	CONCLUSIONS . . . . .	39
	REFERENCES . . . . .	41
	APPENDIX . . . . .	43

## ILLUSTRATIONS

<u>Figure</u>		<u>Page</u>
2-1	Spherical Element Defined by $i^{\text{th}}$ and $j^{\text{th}}$ Nodal Surfaces	4
2-2	Lumped Mass Approximation . . . . .	5
2-3	Integration Technique for Present Finite Element Method	6
4-1	Model Bulk Moduli and Hydrostat . . . . .	12
4-2	Model Bulk Modulus, Hydrostat and Hugoniot Compared with Data . . . . .	12
4-3	Shear Modulus Versus Pressure . . . . .	13
4-4	Triaxial Compression Data and Present Yield Criterion .	14
5-1	Mesh Size and Loading Used in Present Calculations . .	20
5-2	Stress/Time Histories, Cases 1 and 2 . . . . .	22
5-3	Stress/Time Histories, Cases 3 and 4 . . . . .	23
5-5	Stress/Time Histories, Cases 6 and 7 . . . . .	24
5-6	Stress Trajectories at $r/r_0 = 1.015$ . . . . .	26
5-7	Stress Trajectories at $r/r_0 = 2$ . . . . .	27
5-8	Stress Trajectories at $r/r_0 = 3$ . . . . .	27
5-9	Energy Dissipation at $r/r_0 = 2$ . . . . .	29
5-10	Energy Dissipation at $r/r_0 = 3$ . . . . .	30
5-11	Displacement of Cavity Wall . . . . .	31
5-12	Effect of Material Properties and Impulse on Attenuation Rate . . . . .	33
5-13	Effect of Material Properties and Impulse on Attenuation Rate . . . . .	35
6-1	Proposed Loading Programs for Investigating Yield Criteria and Inelastic Deformation on Unloading . . . .	37

PRECEDING PAGE BLANK

## ILLUSTRATIONS (CONTINUED)

<u>Figure</u>		<u>Page</u>
A-1	Input for Jeffreys' Solution . . . . .	44
A-2	Velocity/Time History at $r/r_0 = 2.44$ . . . . .	45
A-3	Coordinates and Pressure/Time History for Ramp Load with Exponential Decay . . . . .	46
A-4	Radial-Stress/Time Histories for Various Rise Times .	55
A-5	Radial-Velocity/Time Histories for Various Rise Times	56
A-6	Effect of Rise Time on Attenuation Rate . . . . .	57

## TABLES

<u>Table</u>		
5-1	Energy Available to Propagate Wave . . . . .	32

## SECTION 1

## INTRODUCTION

Waves are influenced by the constitutive properties of the material in which they propagate. The effects of constitutive properties on spherical wave propagation is of special interest in calculating the effects of underground nuclear explosions. Recent efforts using numerical methods to predict the effects of the PILEDRIVER event have focussed attention on the role of mathematical models of constitutive properties. The purpose of the present paper is to illustrate how various assumptions about constitutive properties affect the calculated wave propagation.

In the present analysis, the finite element method is adapted to spherical geometry. A mathematical model is derived for Cedar City Tonalite based on laboratory measurements. The model contains a bulk modulus which depends on the current density, a shear modulus, a yield criterion and a rule of plastic flow. The Tonalite is considered to be an infinite medium surrounding a cavity which contains a sphere of chemical explosive. Detonation of the explosive is represented by applying a pressure to the surface of the cavity which varies with time in a manner similar to that measured by Physics International Company (Reference 1). The peak pressure used in the present calculations is 31.5 kilobars.

The results of the calculations are presented as stress/time histories and stress/strain relations at various ranges and as rates of attenuation of the peak radial stress. The effects of varying these properties are studied by comparing stress/time histories and stress/strain relations at various ranges and as rates of attenuation of the peak radial stress. The primary comparisons are made among cases where the radial stress applied to the cavity surface and hence the impulse is invariant.

AJA

R-6813-777



## SECTION 2

### FINITE ELEMENT METHOD

The application of the finite element method to problems in continuum mechanics has been thoroughly discussed by previous writers (References 2-4). Hence, only a few subjects pertaining specifically to the present adaptation of the finite element method are discussed below.

The incremental equation of dynamic equilibrium is

$$[m]\{\delta\ddot{u}\} + [c]\{\delta\dot{u}\} + [K]\{\delta u\} = \{\delta P\} \quad (1)$$

In which

- $[m]$  = Global mass matrix
- $[c]$  = Global damping matrix
- $[K]$  = Global (tangent) stiffness matrix
- $\{\delta\ddot{u}\}, \{\delta\dot{u}\}, \{\delta u\}$  = Increments of acceleration, velocity, and displacement
- $\{\delta P\}$  = Increment of load

The global stiffness matrix is assembled from element stiffness matrices  $[k]$ . For a typical element (see Figure 2-1)

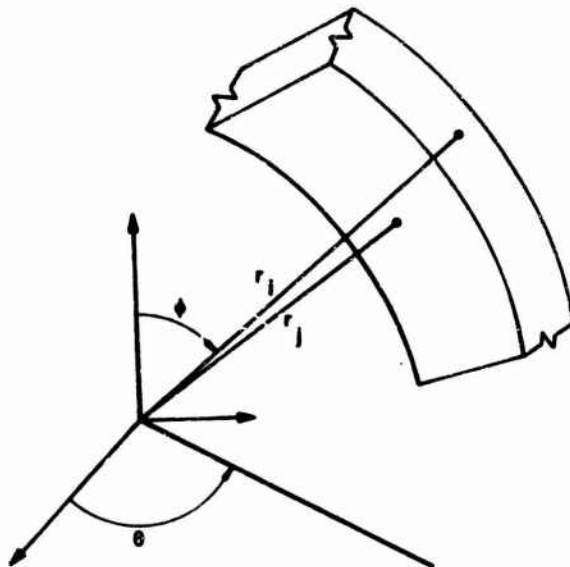
$$[k] = \{[A]^{-1}\}^T \int_{Vol} [B]^T [D] [B] dV [A]^{-1} \quad (2)$$

where  $[A]^{-1}$  = A transformation matrix relating the generalized displacements of the finite element theory to the physical radial displacement

$[B]$  = Strain/displacement transformation matrix

$[D]$  = Matrix of tangent stress/strain moduli relating incremental stress to incremental strain

**PRECEDING PAGE BLANK**



AJA1054

FIGURE 2-1. SPHERICAL ELEMENT DEFINED BY  $i^{th}$  AND  $j^{th}$  NODAL SURFACES

In the present case

$$[A]^{-1} = \frac{1}{\frac{r_i}{r_j^2} - \frac{r_j}{r_i^2}} \begin{bmatrix} \frac{1}{r_j^2} & -\frac{1}{r_i^2} \\ -r_j & r_i \end{bmatrix} \quad (3)$$

where  $r_i, r_j$  = Radii of the  $i^{th}$  and  $j^{th}$  nodal surfaces

$[A]^{-1}$  expresses the displacement  $u$  between the  $i^{th}$  and  $j^{th}$  nodal surfaces by the following equation:

$$u = \langle r \ r^{-2} \rangle [A]^{-1} \begin{Bmatrix} u_i \\ u_j \end{Bmatrix} \quad (4)$$

The displacement function, Equation 2-4, satisfies the elasto-static solution of a hollow sphere subjected to internal and/or external pressure.

The strain components associated with this displacement are

$$\epsilon_r = \frac{\partial u}{\partial r} \quad (5a)$$

$$\epsilon_\theta = \epsilon_\phi = \frac{u}{r} \quad (5b,c)$$

Performing the indicated differentiation shows that

$$\begin{Bmatrix} \epsilon_r \\ \epsilon_\theta \\ \epsilon_\phi \end{Bmatrix} = \begin{bmatrix} 1 & -2r^{-3} \\ 1 & r^{-3} \\ 1 & r^{-3} \end{bmatrix} [A]^{-1} \begin{Bmatrix} u_i \\ u_j \end{Bmatrix} \quad (6)$$

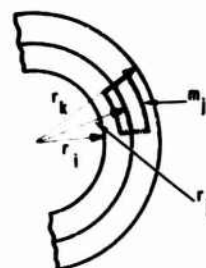
Hence,

$$[B] = \begin{bmatrix} 1 & -2r^{-3} \\ 1 & r^{-3} \\ 1 & r^{-3} \end{bmatrix} \quad (7)$$

Within an element, strain varies as  $1/r^3$ .

The global mass matrix is based on the assumption of lumped mass at nodal surfaces. Each element contributes half of its mass to its two end nodal surfaces as illustrated in Figure 2-2. In the problems to be discussed here, the global damping matrix is assumed to be zero.

The method by which the displacement increment at  $t_0 + \delta t$  is obtained from the known solution at  $t_0$  is based on the assumption of linear acceleration during the time step. The method is based on work by Wilson (Reference 3) and Felippa (Reference 5). The solution is obtained in two



A51053

FIGURE 2-2. LUMPED MASS APPROXIMATION

steps as illustrated in Figure 2-3. In the first step, the solution at  $t_0 + \delta t/2$  is estimated using the known tangent stiffness at  $t_0$ . This is done by obtaining a temporary solution at  $t_0 + \delta t$  (1 in the Figure) and then interpolating to  $t_0 + \delta t/2$  (2 in the Figure). The solution at the end of the first pass is used to evaluate the stiffness matrix  $[K]$  at  $t_0 + \delta t/2$ . The first pass solution is then discarded. The second pass is performed using  $[K]$  at  $t_0 + \delta t/2$  to obtain a temporary solution at  $t_0 + 2\delta t$  (3 in the Figure). The final result is obtained by interpolating between  $t_0$  and  $t_0 + 2\delta t$  to find the incremental displacement at  $t_0 + \delta t$  (4 in the Figure).

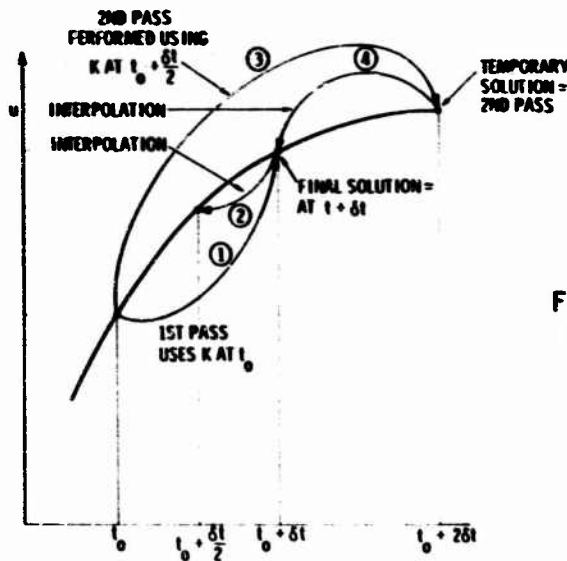


FIGURE 2-3. INTEGRATION TECHNIQUE FOR PRESENT FINITE ELEMENT METHOD

This integration procedure requires the equations of motion to be solved twice during every time step and therefore appears to be more time-consuming than necessary. However, the materials of interest exhibit a large difference in stiffness between loading and unloading, and it was feared that small numerical errors might lead to large changes in stiffness and to instability. Hence, the conservative procedure described above was adopted. The present calculations show that this procedure is stable. However, some recent theoretical work at AJA seems to indicate that a one pass method would be just as effective as the present two pass method. Further work is required to confirm this.

### SECTION 3

#### MATHEMATICAL MODEL OF MATERIAL PROPERTIES

The mathematical model which is used in the present work has the following basic features:

- a. Bulk modulus (B) may be a function of the excess compression  $\mu = \frac{\rho}{\rho_0} - 1$ , where  $\rho$  = current density and  $\rho_0$  = initial density.
- b. Shear modulus (G) may be a function of the current state of stress. In the present examples it is assumed to be constant.
- c. Yield criterion may be a function of the first stress invariant ( $J_1$ ) and of the second invariant of stress deviator ( $J_2'$ ) (Reference 6).
- d. Work-hardening or strain-hardening rules prescribe how the yield criterion may vary as a function of plastic work or plastic strain. In the present examples, hardening is assumed to be zero and the initial yield criterion is a permanent property of the material (Reference 6).
- e. Flow rules prescribe how changes in plastic strain are related to changes in stress when the yield criterion is satisfied. Two flow rules, the plastic potential (Reference 7) and a version of the Prandtl-Reuss rule (Reference 8), are considered.

This mathematical model must be expressed as a matrix of coefficients  $[D]$  relating stress increments  $\{d\sigma\}$  to total strain increments  $\{d\epsilon\}$ .

$$\{d\sigma\} = [D] \{d\epsilon\} \quad (8)$$

The  $[D]$  matrix has two purposes in the finite element scheme described above. One is in formulating the element stiffness matrix  $[k]$ , Equation 2. The

second purpose is in determining the stress increments in the element between the  $i^{th}$  and  $j^{th}$  node from the incremental nodal displacements as indicated by Equation 9.

$$\{d\sigma\} = [D] [B] [A]^{-1} \begin{Bmatrix} du_i \\ du_j \end{Bmatrix} \quad (9)$$

The starting point in deriving [D] is Hooke's law for small strains which relates the incremental stress tensor,  $d\sigma_{ij}$ , to the elastic component of the strain tensor,  $d\epsilon_{ij}^e$ .

$$d\sigma_{ij} = \lambda d\epsilon_{kk}^e \delta_{ij} + 2G(d\epsilon_{ij}^e) \quad (10)$$

where  $\lambda$  = Lamé's parameter,  $B = \frac{2}{3} G$

If the state of stress does not satisfy the yield criterion, the elastic strain increment and the total strain increment are equal and [D] is based on Equation 10. However, if the yield criterion is satisfied, further computations are necessary to obtain [D].

Defining the elastic strain increment as the difference between the plastic strain increment,  $d\epsilon_{ij}^p$ , and the total strain increment,  $d\epsilon_{ij}$ , Equation 10 may be rewritten as follows:

$$d\sigma_{ij} = \lambda (d\epsilon_{kk} - d\epsilon_{kk}^p) \delta_{ij} + 2G(d\epsilon_{ij} - d\epsilon_{ij}^p) \quad (11)$$

The flow rule is used to express  $d\epsilon_{ij}^p$  in terms of the yield criterion and components of the stress or stress deviator tensor

$$d\epsilon_{ij}^p = \lambda \frac{\partial f}{\partial \sigma_{ij}} \quad (\text{plastic potential}) \quad (12a)$$

$$d\epsilon_{ij}^p = \lambda \frac{\partial f}{\partial \sigma_{ij}} \quad (\text{present version of Prandtl-Reuss flow rule}) \quad (12b)$$

For the sake of simplicity in the following derivation, both Equations 12a, b are expressed as

$$d\epsilon_{ij}^p = \Lambda f_{ij} \quad (13)$$

In the subsequent applications of the mathematical model it is made clear which flow rule is being used.

From the assumption of no work or strain hardening, it follows that there is no change in the yield function. The mathematical statement of this assumption is

$$d(f(\sigma_{ij})) = 0 \quad (14a)$$

or

$$\frac{\partial f}{\partial \sigma_{ij}} d\sigma_{ij} \equiv f_{ij} d\sigma_{ij} = 0 \quad (14b)$$

Substituting Equation (11) into Equation (14b) and making use of Equation (13) leads to the following equation.

$$\lambda (d\epsilon_{kk} - \Lambda f_{kk}) \delta_{ij} f_{ij} + 2G (d\epsilon_{ij} - \Lambda f_{ij}) f_{ij} = 0 \quad (15)$$

The scalar quantity  $\Lambda$  may be found by rearranging Equation 15.

$$\Lambda = \frac{\lambda (d\epsilon_{kk}) (f_{\ell\ell}) + 2G (d\epsilon_{ij}) (f_{ij})}{\lambda (f_{kk}) (f_{\ell\ell}) + 2G (f_{ij}) (f_{ij})} \quad (16)$$

Making use of Equation (16) in Equation (13) and substituting the result into Equation (11), the stress increment is expressed in terms of the total strain increment and the total stresses. This is the desired result.

The remaining task is to factor out coefficients in the  $[D]$  matrix, which is given on the following page.

$$[D] = \begin{bmatrix} \lambda + 2G - \frac{(\lambda F + 2Gf_r)^2}{\lambda F^2 + 2Gx} & \lambda - \frac{(\lambda F + 2Gf_\theta)(\lambda F + 2Gf_r)}{\lambda F^2 + 2Gx} & \lambda - \frac{(\lambda F + 2Gf_z)(\lambda F + 2Gf_r)}{\lambda F^2 + 2Gx} \\ & \lambda + 2G - \frac{(\lambda F + 2Gf_\theta)^2}{\lambda F^2 + 2Gx} & \lambda - \frac{(\lambda F + 2Gf_\theta)(\lambda F + 2Gf_z)}{\lambda F^2 + 2Gx} \\ & & \lambda + 2G - \frac{(\lambda F + 2Gf_z)^2}{\lambda F^2 + 2Gx} \end{bmatrix}$$

Symmetrical

(17)

where

$$F = f_r + f_\theta + f_\phi$$

$$x = f_r^2 + f_\theta^2 + f_\phi^2$$

$f_r$ , etc. = Derivatives of the yield function  $f$  with respect to stress components (plastic potential flow rule) or stress deviator components (present version of Prandtl-Reuss flow rule).  $f_r$  indicates differentiation with respect to radial stress or stress deviator component.



# SECTION 4

## PROPERTIES OF ROCK USED IN FINITE ELEMENT CALCULATIONS

Specific material properties were derived from a variety of laboratory tests on Cedar City Tonalite and NTS granite. Properties of both rocks are incorporated into the model, which is intended to represent a weathered granite.

### BULK MODULUS

The mathematical model of bulk modulus is based on hydrostatic compression tests in the range 0-37 kilobars (Reference 9, 10). Release adiabatic data (Reference 11) were also taken into account when deciding that hysteresis should be incorporated into the model. The model, which is intended for use only when  $\mu = \frac{\rho}{\rho_0} - 1$  is positive, is given below.

Loading ( $\mu \geq \mu_{\max}$ , the previous maximum  $\mu$  in a particular element)

$$B = B_{ult} - (B_{ult} - B_0) \exp\left(\frac{-\mu}{\mu_1}\right) \quad (18)$$

Unloading or reloading ( $\mu > \mu_{\max}$ )

$$B = B_u + (B_{ult} - B_u) \left(\frac{\mu}{\mu_2}\right) \quad (19)$$

$$\text{and } B_u = \text{the lesser of } \begin{cases} B_0 + (B_{ult} - B_0) \frac{\mu_{\max}}{\mu_2} \\ B_{ult} \end{cases} \quad (20)$$

The empirical coefficients in these equations are as follows:

$$\begin{aligned} B_{ult} &= 7.6 \times 10^6 \text{ psi} & \mu_1 &= 0.0275 \\ B_0 &= 1.205 \times 10^6 \text{ psi} & \mu_2 &= 0.05 \end{aligned}$$

Bulk moduli for typical cycles of loading and unloading are shown in Figure 4-1 and the model is compared with experimental data in Figure 4-2.

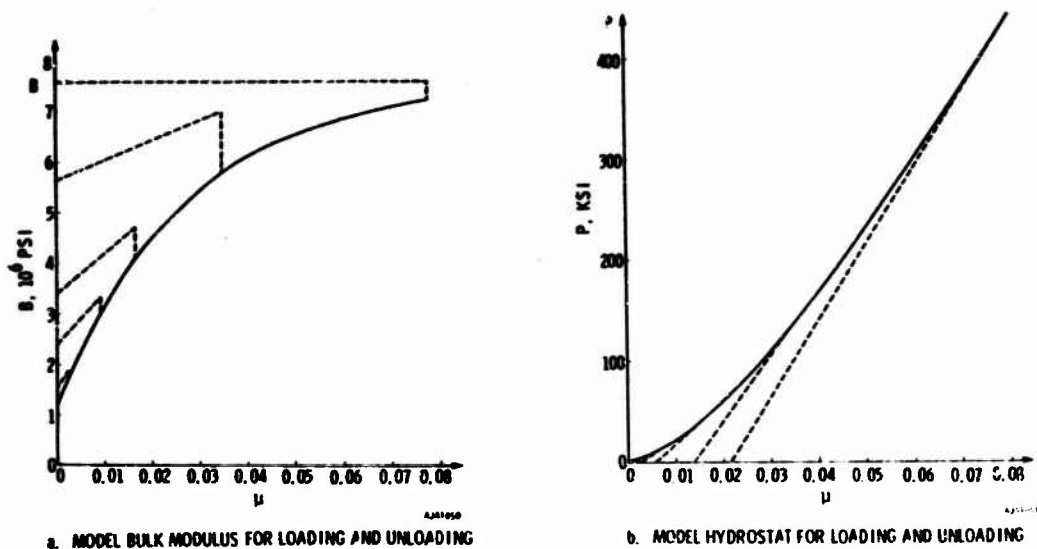


FIGURE 4-1. MODEL BULK MODULI AND HYDROSTAT

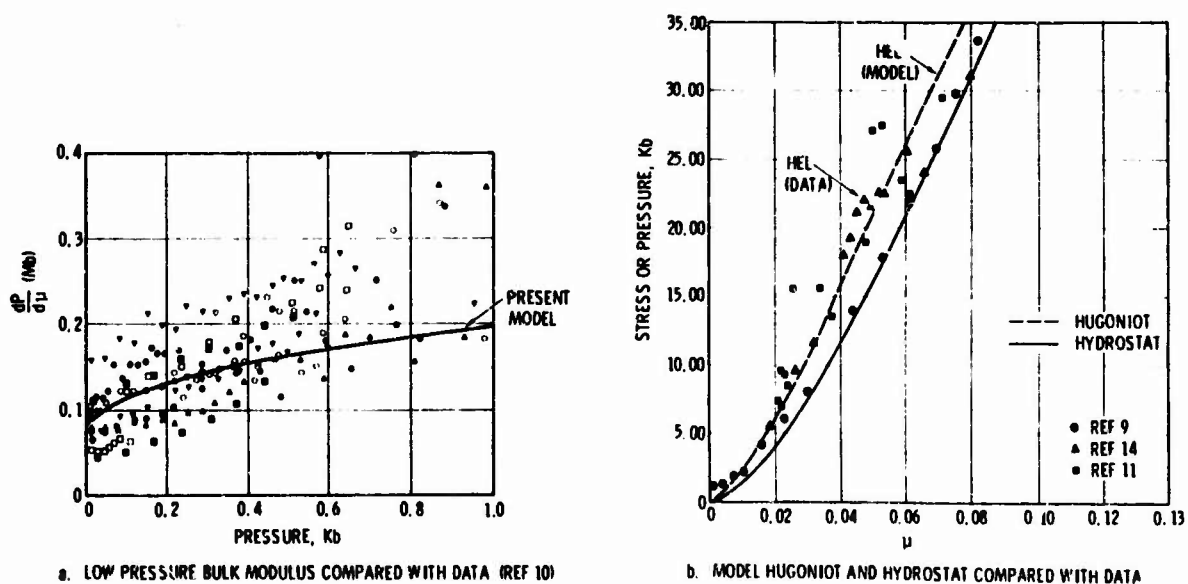


FIGURE 4-2. MODEL BULK MODULUS, HYDROSTAT AND HUGONIOT COMPARED WITH DATA

## SHEAR MODULUS

The model shear modulus is based on the slope of deviatoric stress/strain curves measured during triaxial compression tests on Cedar City Tonalite (Reference 10). The data, which are shown in Figure 4-3 seem to indicate that  $G$  decreases with increasing confining pressure. The trend is too weak to justify a model which is more complicated than  $G = \text{a constant}$ . However, the  $G$  which is chosen

$$G = 0.69 \text{ kb} \approx 10^6 \text{ psi}$$

gives more weight to the data at the high pressure end of the range of measurements.

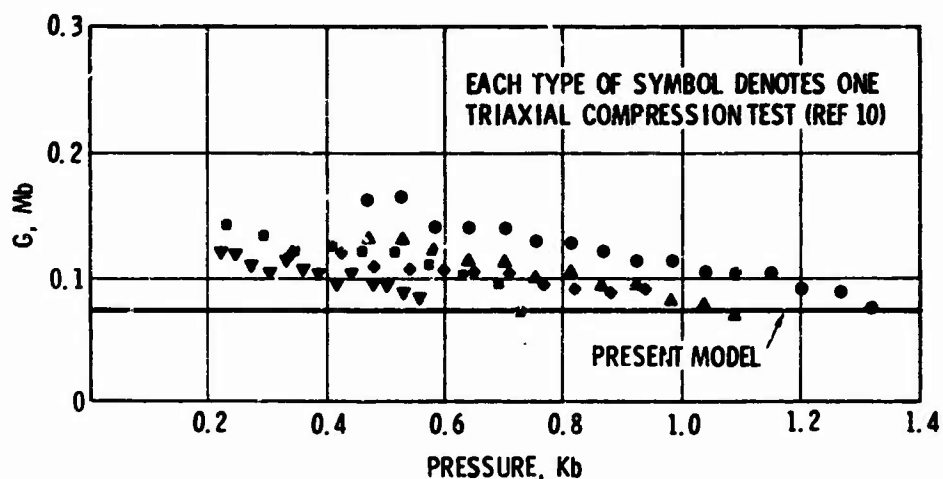


FIGURE 4-3. SHEAR MODULUS VERSUS PRESSURE

## YIELD CRITERIA

The yield criterion, which has the form

$$f = \sqrt{J_2} - \alpha J_1 - c \leq 0$$

is based on several types of experimental data. The yield criterion at low pressure is based on static, triaxial compression experiments which were

conducted on samples whose minimum dimension was 1 to 2 in. Data obtained from presawn samples of Nevada Test Site granite (Reference 12) and Cedar City Tonalite (Reference 10) and from intact samples of Westerly granite (Reference 13) and Cedar City Tonalite (Reference 10) were considered. The reason for considering presawn samples, which were sawn through at angles of 45-60 deg to the direction of major principal stress, is to try to take into account preexisting cracks in the Physics International specimens and the faults and joint planes which exist in large rock masses in situ.

The data on which the yield criterion is based are shown in Figure 4-4.

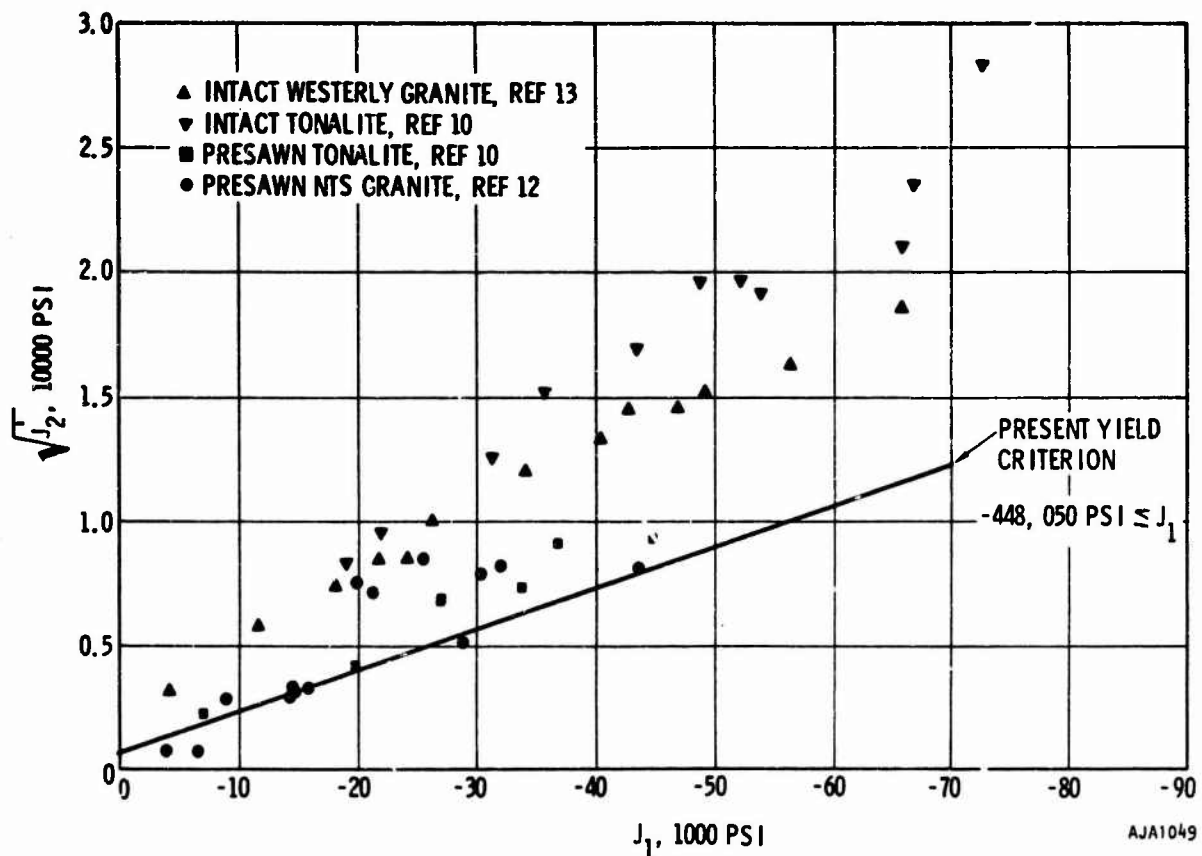


FIGURE 4-4. TRIAXIAL COMPRESSION DATA AND PRESENT YIELD CRITERION

A lower limit on shear strength in the range of the data is used for the yield criterion in the present calculations. The purpose of this is to use a physically plausible yield criterion while allowing a maximum amount of material to undergo inelastic deformation. The coefficients defining the present criterion are as follows.

$$\alpha_1 = -0.157$$

$$c_1 = 1450 \text{ psi}$$

This criterion is assumed to apply in the following range of mean stress.

$$-149,350 \text{ psi} \leq \frac{J_1}{3} = p$$

The criterion implies that the maximum allowable deviatoric stress is zero when  $p = \frac{J_1}{3} = 1900 \text{ psi}$ . The material has a strength under uniaxial tensile stress of 2500 psi, which is too large to be a good representation of weathered granite. A preliminary study indicated that the attenuation of peak stress and general shape of the compressive phase of the pulse varied little as the details of the tensile properties were varied. Hence, the present Coulomb yield criterion plus the restriction that the mean tensile stress may never exceed 1900 psi were adopted for simplicity.

The yield criterion which is assumed to apply in the region  $\frac{J_1}{3} = p < -149,350 \text{ psi}$  is the von Mises type

$$\alpha_2 = 0$$

$$c_2 = 76,000 \text{ psi}$$

This criterion is based on the hypothesis that the rock has an ultimate shear strength depending on the strength of minerals within grains and is independent of friction between grain boundaries. The idea of using a von Mises yield criterion is further supported by the data in Figure 4-2, which indicate that the hugoniot is approximately a constant distance equal to about 90,000 psi above the hydrostat for  $\mu \geq 0.05$ . This is consistent with a value of  $c_2 = 76,000$  psi.

The mean stress at which the transition from Coulomb to von Mises yield criterion is made is determined by using the criterion giving the minimum allowable  $\sqrt{J_2}$ .

$$\sqrt{J_2} = \min \begin{cases} \alpha_1 J_1 + c_1 \\ c_2 \end{cases}$$

One feature of the model which does not agree with the experimental data is the hugoniot elastic limit (HEL in Figure 4-2), defined as the stress level at which a wave propagating in the material has more than one characteristic speed. Although this definition is somewhat inadequate in that it overlooks diffusion, rate effects and compaction at low stress levels, there seems to be a distinct stress level in Tonalite where the wave speed alters appreciably. This has been reported experimentally at about  $\mu = 0.048$  or  $\sigma_1 = -320,000$  psi (Reference 14). In the present model, it occurs at about  $\mu = 0.066$  and  $\sigma_1 = -435,000$  psi. One way to bring this aspect of the model into better agreement with the experimental data is to increase the shear modulus to  $G = 1.5 \times 10^6$  psi. This would also bring the shear modulus into better agreement with low pressure data, and in calculations it would indicate more inelastic deformation on loading than does the present model. The overall effect on the present series of calculations of making such a change would probably be small, however.

# AJA

R-6813-777

## DENSITY

It is assumed that the initial density of the material  $\rho_0 = 2.55 \text{ gm/cm}^3 = 0.000238 \text{ lb} \cdot \text{sec}^2/\text{in.}^4$ . This value is representative of a number of samples taken from the Cedar City site.

## PREVIOUS WORK

The mathematical model of weathered granite used here is adapted from previous work reported in Reference 15.

AJA

R-6813-777



## SECTION 5

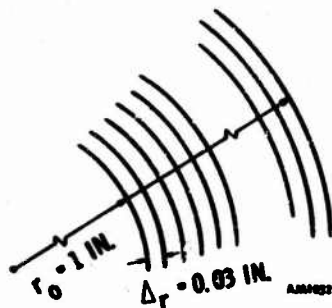
## NUMERICAL RESULTS

Calculations were performed in which the cavity size and pressure/time history applied to the surface of the cavity are comparable to those in physical experiments conducted by Physics International Company, Reference 1. The finite-element grid used in the present calculations is shown in Figure 5-1a. The pressure/time history for the present calculation, Figure 5-1, is adapted from a radial-stress/time history which was measured in a spherical wave experiment on Cedar City Tonalite where the wave was generated by detonating chemical explosive.

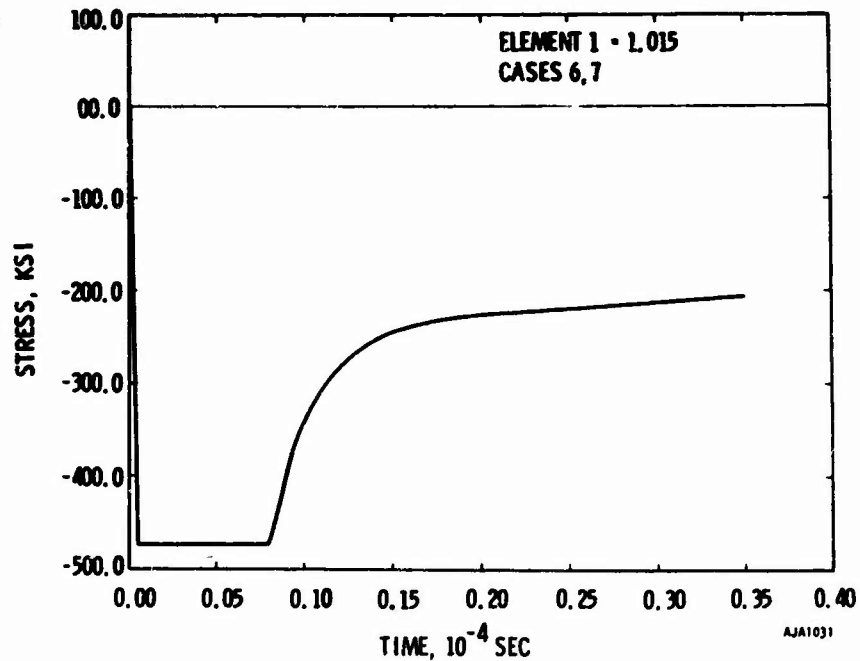
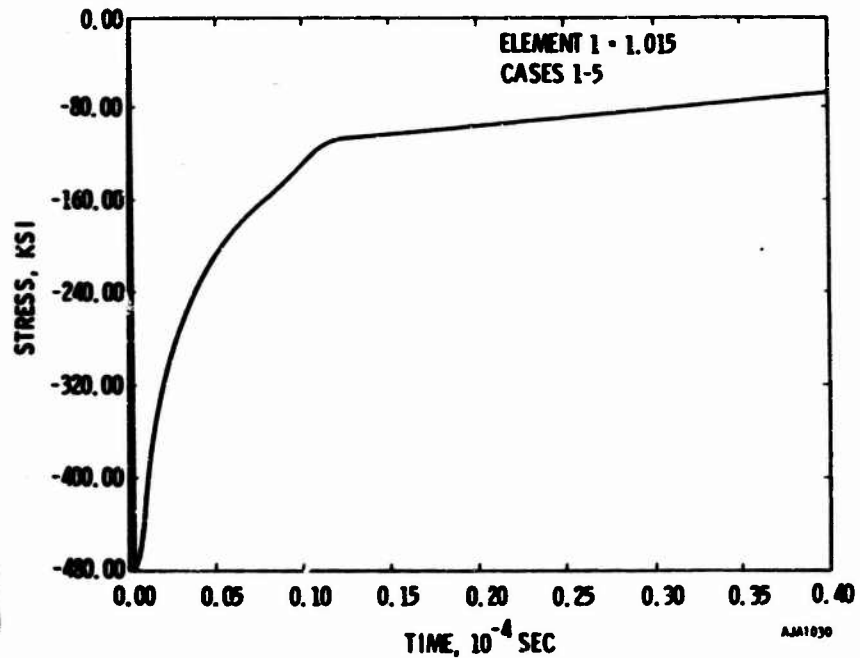
The purpose of using the fine mesh illustrated in Figure 5-1a is to try to maintain the correct rise time of the wave. The rise time, as indicated by measurements in the physical experiment which are reliable to the nearest  $0.1 \times 10^{-6}$  sec is about  $0.7 \times 10^{-6}$  sec. As should be expected in a numerical solution method of the type used here, the rise time increases to  $2.0 - 3.0 \times 10^{-6}$  sec by the time the wave has propagated a distance equal to  $5 \times r_0$ , where  $r_0$  is the cavity radius. A somewhat greater increase in rise time is noticed in the physical experiment, which is probably due either to viscous properties of the material or to dispersion caused by small-scale inhomogeneities in the rock structure.

The reason for trying to represent the correct rise time is that, in the vicinity of the cavity, the rise time influences the rate of attenuation of peak radial stress and particle velocity. This point is discussed in detail in Appendix A. The rate of attenuation is a parameter of practical interest and is used in the present analysis as one index of the effect of changing a particular material property. Hence it is important for the rise time in the numerical calculations to be a physically meaningful quantity and for it to be the same from one computation to the next. Hence, a conservative integration time step  $\delta t = 5 \times 10^{-8}$  sec and a fine finite-element mesh were used.

**PRECEDING PAGE BLANK**



a. FINITE ELEMENT MESH SIZE



b. PRESSURE/TIME HISTORY AT CAVITY WALL

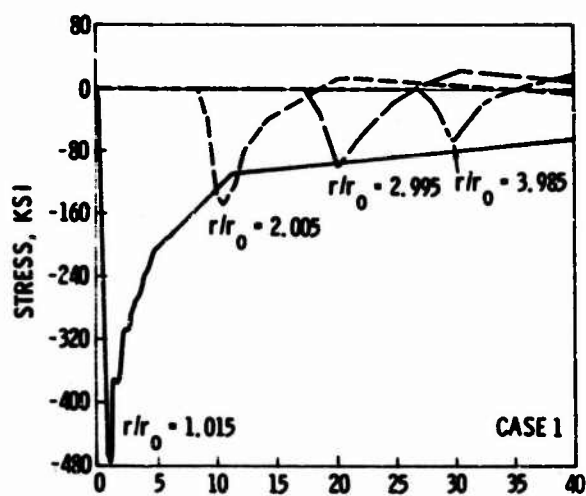
FIGURE 5-1. MESH SIZE AND LOADING USED IN PRESENT CALCULATIONS

The main results of the present study were obtained from a series of seven calculations which are described in the following table.

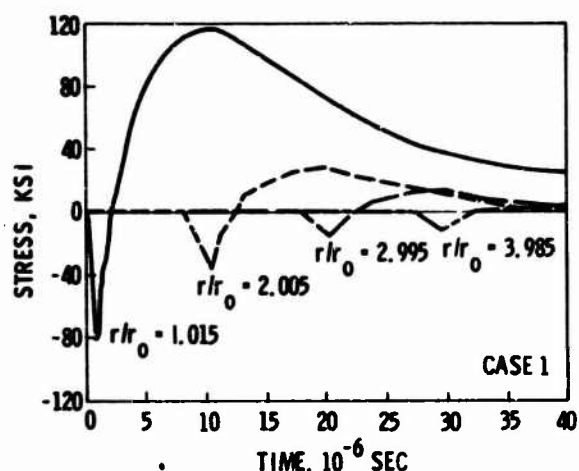
<u>Case</u>	<u>Description</u>
1	Linear elastic (no yield condition imposed); $B = B_0 = 1.2 \times 10^6$ psi; $G = 1 \times 10^6$ psi
2	Variable modulus (no yield condition imposed); B defined by Equations 18-20; $G = 1 \times 10^6$ psi
3	Variable modulus as in Case 2 with von Mises yield criterion ( $\alpha = 0$ , $c = 76125$ psi)
4	Variable modulus as in Case 2 with Coulomb yield criterion ( $\alpha = -0.167$ , $c = 1450$ psi) at $p > -14.5$ kb and von Mises criterion ( $\alpha = 0$ , $c = 76125$ psi) at $p < -14.5$ kb. Plastic Potential flow rule is used.
5	Same as Case 4, except that Prandtl-Reuss flow rule is used.
6	Same as Case 4, except that impulse is increased by a factor of 2.
7	Same as Case 2, except that impulse is increased by a factor of 2.

## STRESS/TIME HISTORIES

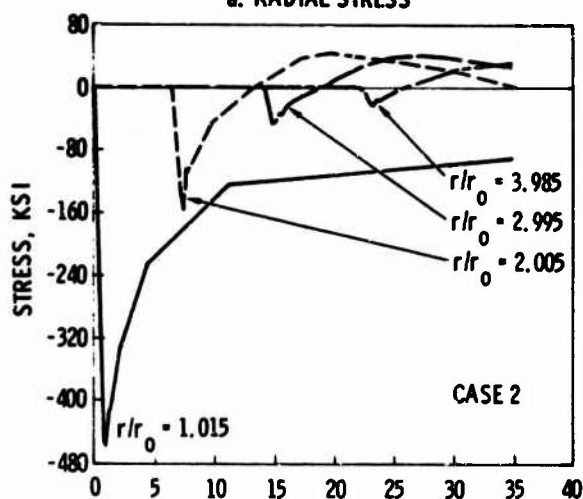
The radial and circumferential-stress/time histories at various ranges from the cavity wall are shown for each case in Figures 5-2 to 5-5. Compressive stresses are defined to be negative. The time duration of each calculation is  $35 \times 10^{-6}$  sec, which allows a fairly complete picture of the stress pulse in the range  $r/r_0 = 1-4$ .



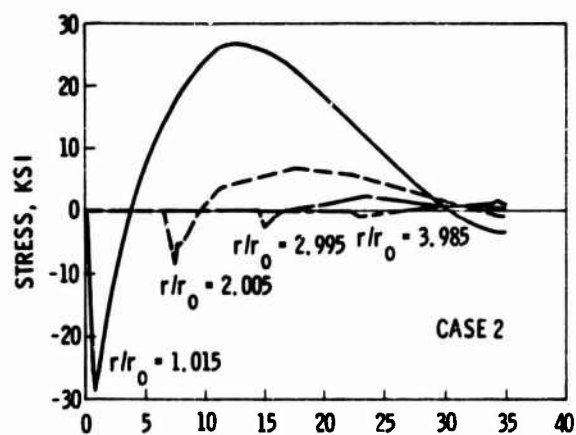
a. RADIAL STRESS



b. CIRCUMFERENTIAL STRESS



c. RADIAL STRESS



d. CIRCUMFERENTIAL STRESS

AJA1255

FIGURE 5-2. STRESS/TIME HISTORIES, CASES 1 AND 2

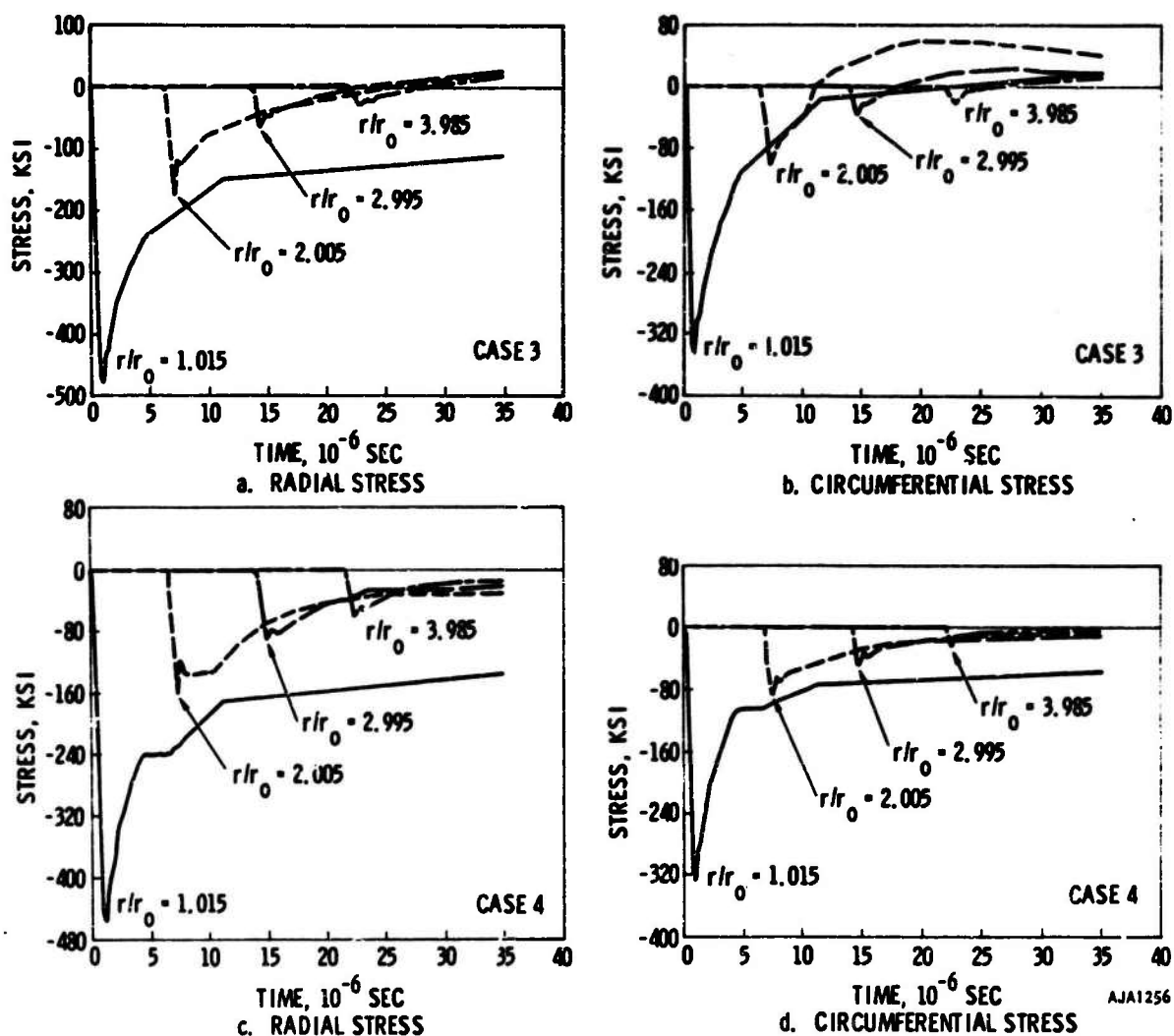


FIGURE 5-3. STRESS/TIME HISTORIES, CASES 3 AND 4

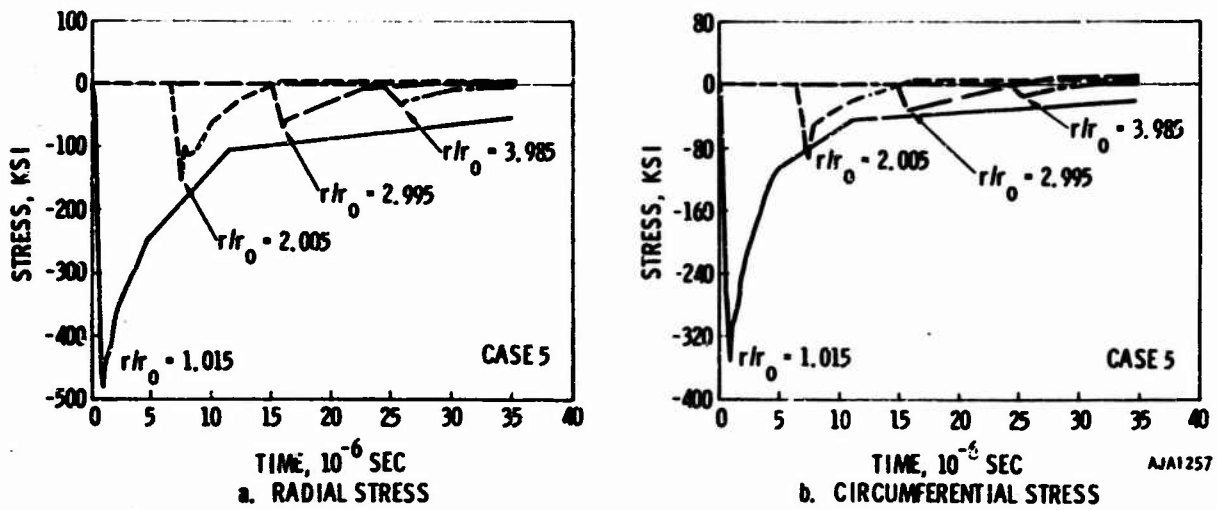


FIGURE 5-4. STRESS/TIME HISTORIES, CASE 5

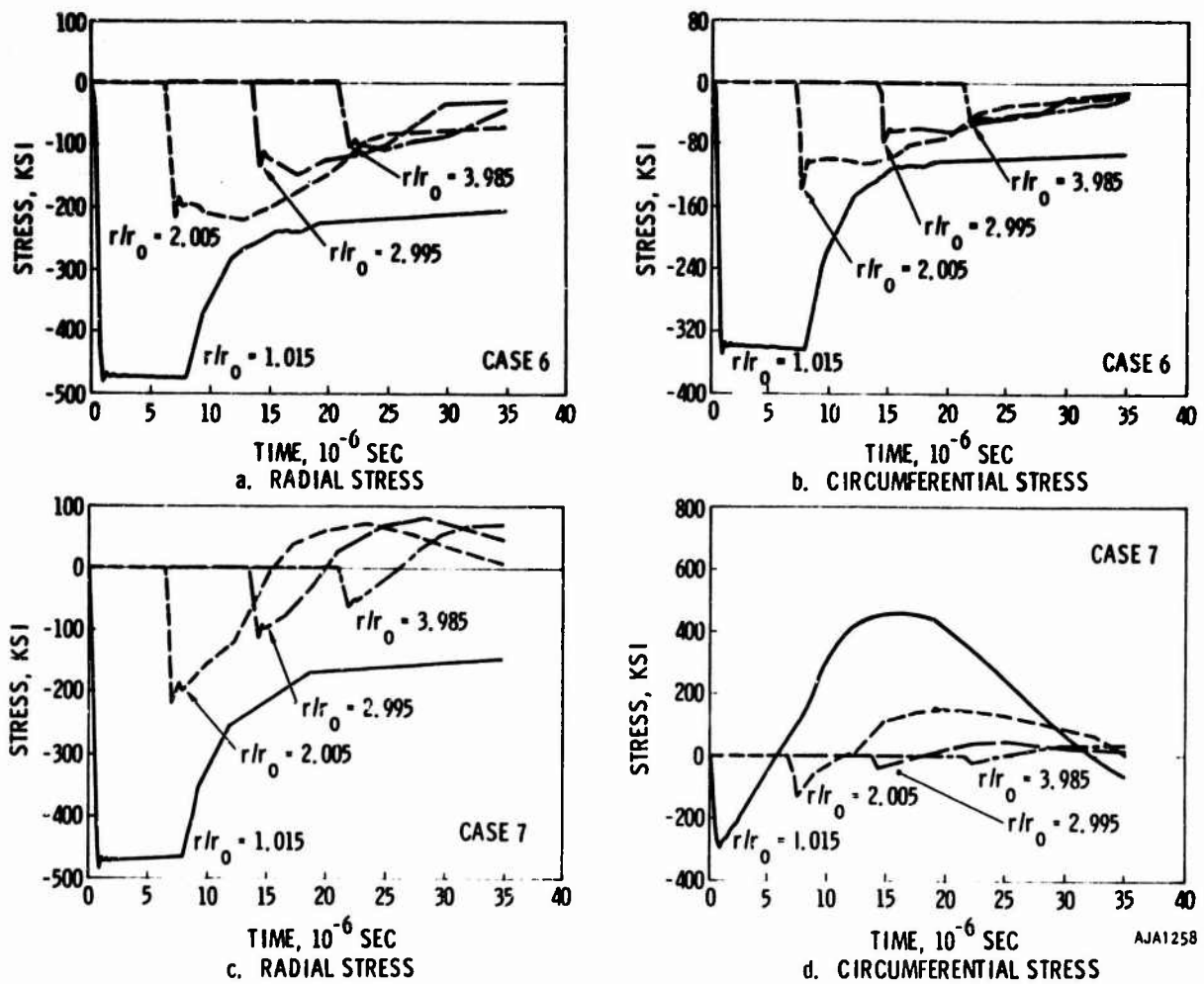


FIGURE 5-5. STRESS/TIME HISTORIES, CASES 6 AND 7

HOOP TENSILE STRESS

The hoop stresses ( $\sigma_\theta$ ,  $\sigma_\phi$ ) are tensile or compressive according to the sense of the elastic component of hoop strain. In spherical waves, the hoop strains ( $\epsilon_\theta$ ,  $\epsilon_\phi$ ) tend to become tensile due to outward radial displacement ( $u$ ) according to the following equation

$$\epsilon_\theta = \epsilon_\phi = u/r$$

Since in the present calculations the rise time of radial stress and particle velocity is very short,  $u=0$  at the time of peak  $\sigma_r$ . The state of strain at this time is approximately uniaxial compression in the  $r$ -direction, and hence compressive  $\sigma_\theta$ ,  $\sigma_\phi$  are induced by Poisson's ratio effects just as they are in plane wave propagation. This behavior is governed by the material properties and wave shape used in the present calculations. The hoop stress would be initially tensile if Poisson's ratio were assumed to be zero, and the amplitude and duration of the compressive hoop stress would be reduced if the rise time were lengthened.

Following an initial compressive phase,  $\sigma_\theta$ ,  $\sigma_\phi$  become tensile in the linear elastic and variable modulus cases (Cases 1 and 2). In Case 3,  $\sigma_\theta$ ,  $\sigma_\phi$  at  $r/r_0 = 1.015$  are influenced by the development of plastic deformation, during which the effective Poisson's ratio is 0.5. The component of hoop strain due to Poisson's ratio effects is thus larger than in Cases 1 and 2, and outward displacement must be correspondingly larger before  $\sigma_\theta$ ,  $\sigma_\phi$  can become tensile. This accounts for the occurrence of tensile stresses at about  $t = 22 \times 10^{-6}$  sec in Case 3. At ranges greater than about  $r/r_0 = 1.75$ , the yield criterion is no longer satisfied in Case 3 and  $\sigma_\theta$ ,  $\sigma_\phi$  become similar to those in Cases 1 and 2.

In Case 4, tensile stresses do not occur anywhere within the range considered. Part of the reason for this behavior is the Coulomb yield condition which allows plastic deformations to occur at relatively low stress levels and large ranges. Also, dilatency or plastic volume increase takes place during unloading. In the range of this problem, outward displacement is not large enough to absorb all this dilatency, and so hoop compressive stresses are induced.

This effect of dilatency is further illustrated in Case 5, where the Coulomb yield criterion is used but plastic dilatency is not allowed. The low yield criterion suppresses tensile stresses at  $r/r_0 = 1.015$ , but at greater ranges, tensile stresses develop for the same reason as in Cases 1-3.

## $\sigma_r/\sigma_\theta$ TRAJECTORIES

Plots of  $\sigma_r$  vs  $\sigma_\theta$ ,  $\sigma_\phi$  further illustrate the influence of the yield criterion on the wave shape. Figures 5-6 to 5-8 show  $\sigma_r/\sigma_\theta, \sigma_\phi$  trajectories at  $r/r_0 = 1.015$ , 2.00 and 3.00. Superposed on each figure are yield criteria used in Case 3 (von Mises) and Cases 4, 5 (von Mises at  $p < 14.5\text{kb}$ ; Coulomb elsewhere). In Cases 1 and 2, the stress path is unrestrained by a yield criterion. The ratio of  $\sigma_r/\sigma_\theta$  is greater in Case 1 than in Case 2 because Poisson's ratio in Case 1 is smaller. In Case 2, Poisson's ratio tends toward 0.45 as the bulk modulus  $B$  tends toward its maximum value of  $7.6 \times 10^6$  psi. This causes the material in Case 2 to appear more fluid-like than in Case 1. Hence the stress state in Case 2 lies nearer the hydrostat.

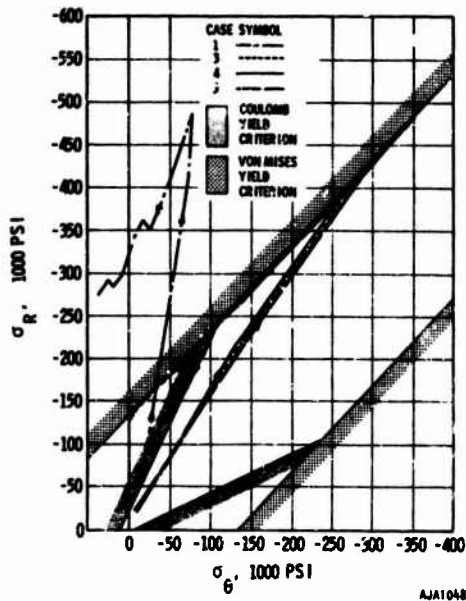


FIGURE 5-6. STRESS TRAJECTORIES AT  $r/r_0 = 1.015$



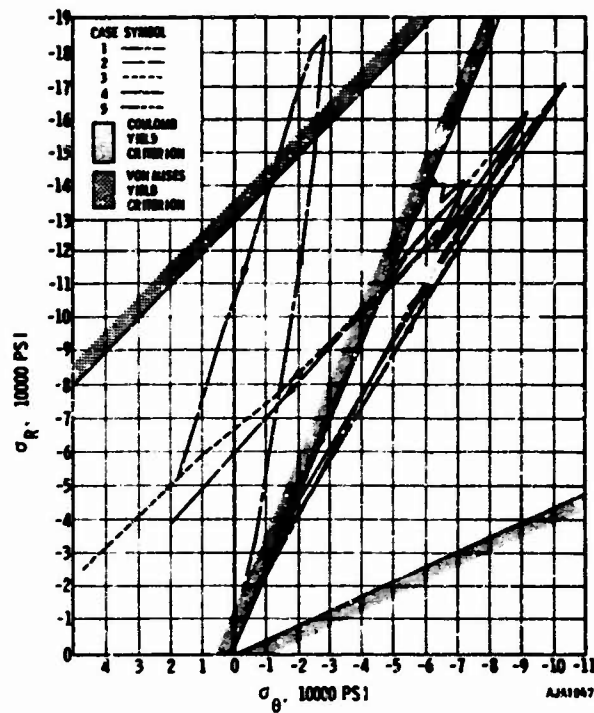


FIGURE 5-7. STRESS TRAJECTORIES AT  $r/r_0 = 2$

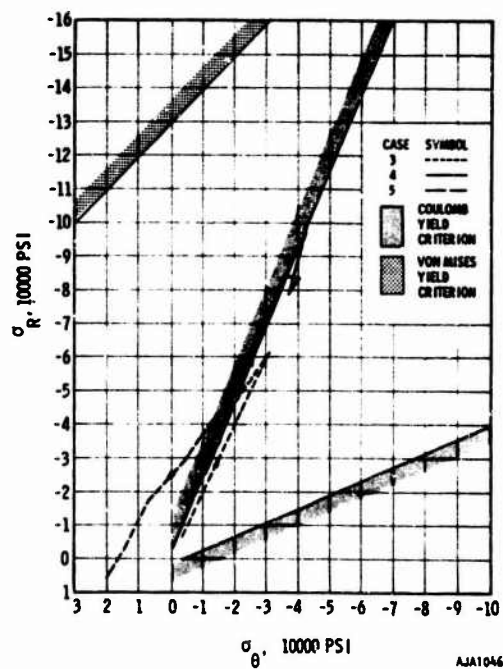


FIGURE 5-8. STRESS TRAJECTORIES AT  $r/r_0 = 3$

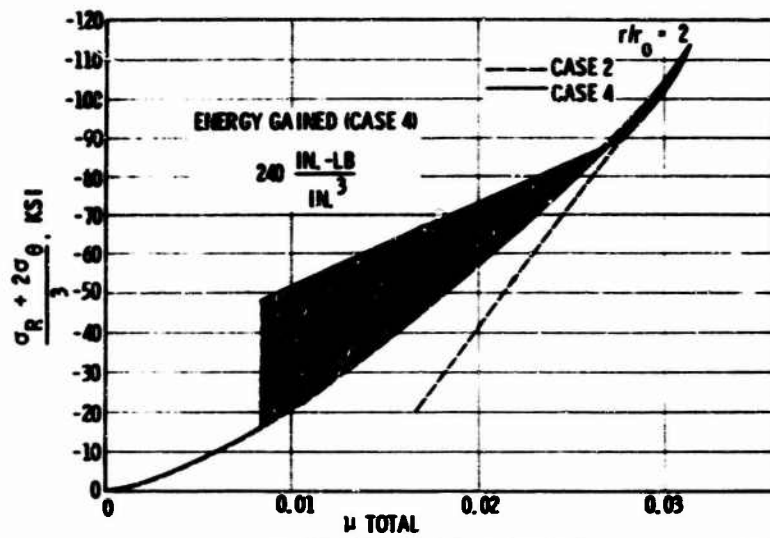
The trend which is exhibited in Case 2 also appears in Cases 3, 4, and 5. For example, at  $r/r_0 = 2$ , the peak stress in all cases lies inside the yield surface. Frequently, at greater ranges only the peak or only the toe of the stress wave lies on the yield surface. A major feature of the present calculations is the absence of sustained plastic deformation on loading.

In contrast, unloading is frequently accompanied by significant plastic deformation. The outward displacement which accompanies any compression wave caused  $\sigma_\theta$  to unload more rapidly than  $\sigma_r$ . The result is that the stress point in  $\sigma_r/\sigma_\theta$  plane tends away from the hydrostat on the  $\sigma_r$  side until it encounters the yield surface. During subsequent plastic unloading,  $\sigma_r$  remains the major principal stress. This behavior is distinctly different from the one-dimensional strain case, in which the major principal stress during plastic unloading is at some stages perpendicular to the direction of wave propagation.

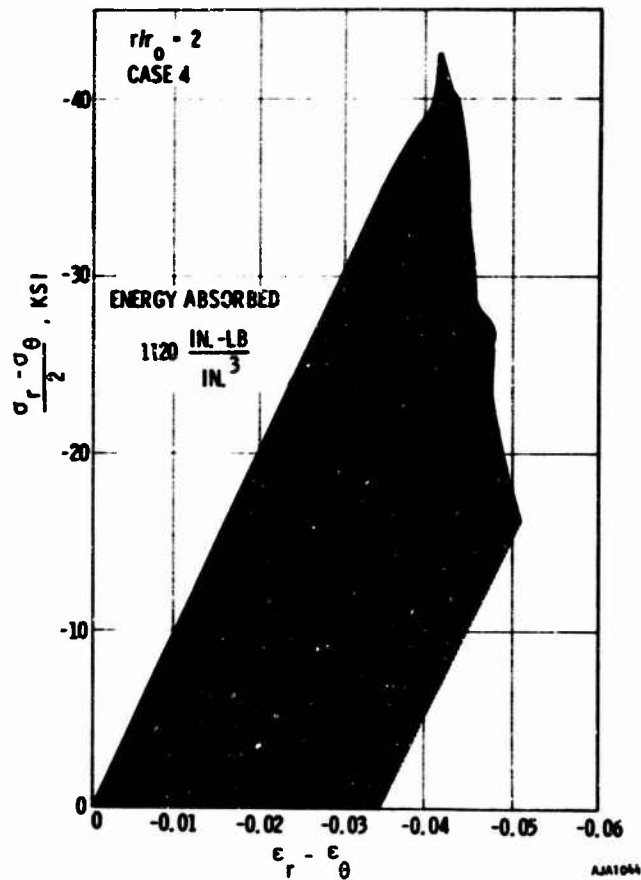
#### DILATENCY AND $\tau/\gamma$

Plastic deformation in Case 4 is associated with dilatency, or plastic volumetric expansion. By far the largest amount of plastic deformation, and hence dilatency, takes place during unloading. This is illustrated in Figures 5-9 and 5-10 where the  $P/\mu$  curves for Case 4 are compared with those in Case 2 at  $r/r_0 = 2$  and 3. Dilatency causes the unloading  $P/\mu$  curve to lie above the loading curve. Thus, during most of the unloading phase, the bulk modulus is less than either the loading or the unloading bulk moduli in the absence of plasticity. This behavior, in conjunction with inelastic deformation in shear, reduces the speed of the unloading wave and therefore contributes to a slower rate of attenuation of the peak  $\sigma_r$  for Case 4 than for other inelastic cases.

Although the unloading  $P/\mu$  curve is above the loading curve, there is net energy dissipation in the material. This is demonstrated in Figures 5-9 and 5-10, where the areas under the shear stress/strain curves at  $r/r_0 = 2$  and 3, representing absorption of inelastic energy, are greater than the areas between the loading and unloading  $P/\mu$  curves.

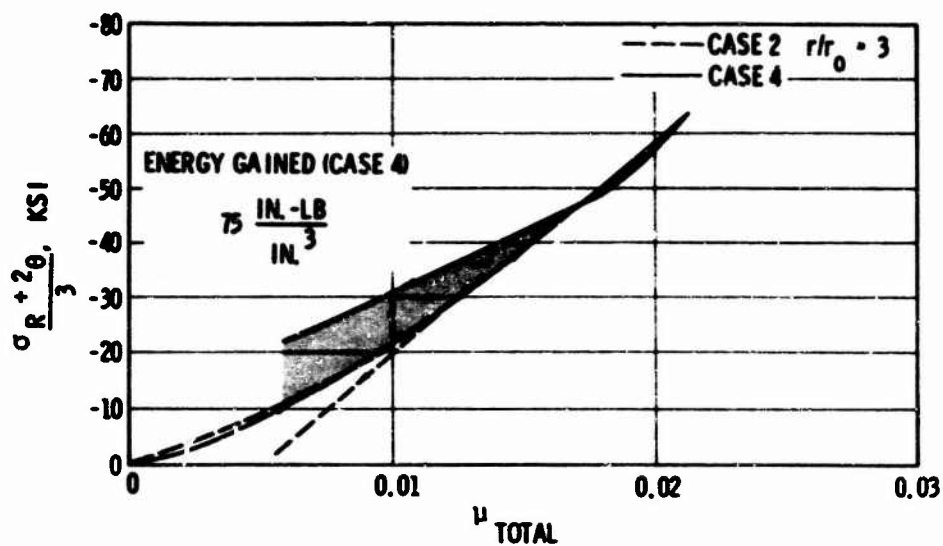


a. MEAN STRESS/STRAIN RELATION



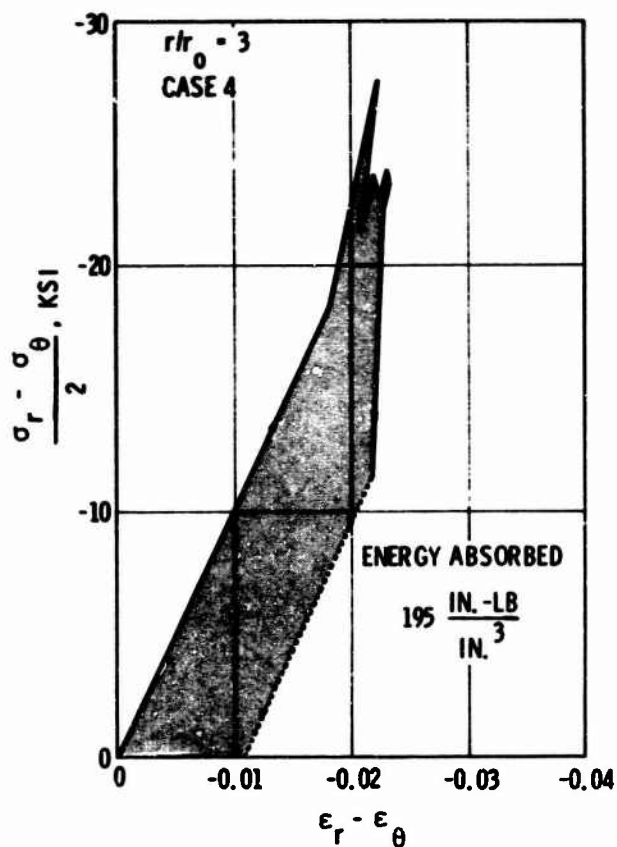
b. DEVIATORIC STRESS/STRAIN RELATION

FIGURE 5-9. ENERGY DISSIPATION AT  $r/r_0 = 2$



a. MEAN STRESS/STRAIN RELATION

AJA1043



b. DEVIATORIC STRESS/STRAIN RELATION

AJA1042

FIGURE 5-10. ENERGY DISSIPATION AT  $r/r_0 = 3$

GROWTH OF CAVITY

The amount of cavity expansion is a reflection of the material properties and the amount of energy originally available to propagate the wave. The displacement of the cavity surface in Cases 1-5 is shown as a function of time in Figure 5-11. Plastic deformation in Cases 3-5 is apparently responsible for the large expansion. One reason that the expansion in Case 3 is less than in Cases 4 and 5 is that the yield criterion in Case 3 permits hoop stresses to tend toward tension whereas the criteria in Cases 4 and 5 maintain compressive hoop stress at the cavity wall. The second reason is that more yielding occurs in Cases 4 and 5 because the yield criteria are satisfied at a lower stress level.

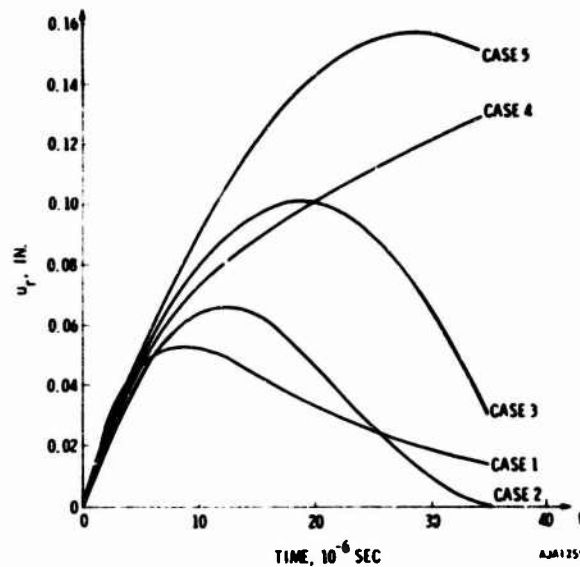


FIGURE 5-11. DISPLACEMENT OF CAVITY WALL

ATTENUATION RATES

The rate at which peak radial stress attenuates with range is a common index of the material properties and wave behavior. The stress at the front of a spherically-diverging step wave propagating in an elastic material attenuates at a rate proportional to  $r^{-1}$  (Reference 16). Inelasticity may accelerate attenuation by allowing unloading signals to overtake the front and by absorbing energy of the wave.

The interpretation of attenuation rates in the present work is complicated since each case has a different amount of energy initially available to propagate the wave. This happens because a common pressure/time history acts through different displacements of the cavity wall. The amount of energy initially available to the wave in each case is shown in Table 5-1.

TABLE 5-1. ENERGY AVAILABLE TO  
PROPAGATE WAVE

Case	$U/U_0$
1	1
2	1.03
3	1.52
4	2.61
5	2.69
6	8.95
7	4.25

$$U_0 = 0.127 \times 10^6 \text{ in.-lb}$$

The attenuation rates of peak radial stress in Cases 1-5 are shown in Figure 5-12. Comparison between Cases 1 and 2 indicates that adding volumetric hysteresis strongly increases the attenuation rate. This is because volumetric hysteresis absorbs some of the energy of the wave and because the unloading signals travel faster than the loading signals, overtaking the peak and degrading it. Interpretation of Case 4 is complicated

because there is considerably more energy initially available to propagate the wave than in Cases 1 and 2, but the material of Case 4 is also much more dissipative. The slow attenuation rate of the peak in Case 1 appears not to be due to the extra energy in the wave, which is primarily associated with the portion of the wave behind the peak, but instead to the reduction in the speed of unloading signals caused by dilatency. This is due to reduction in the effective bulk modulus caused by dilatency as illustrated in Figures 5-9a and 5-10a.

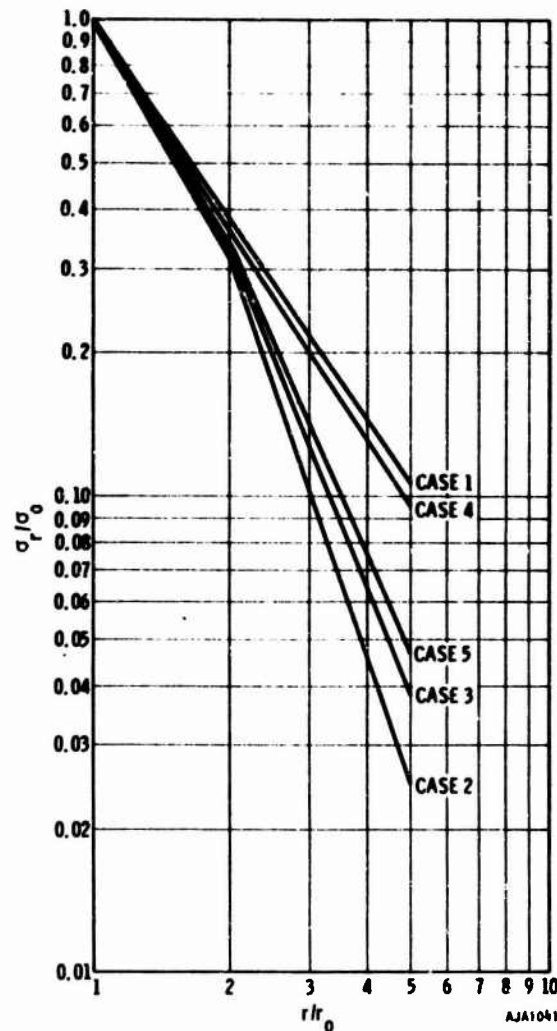


FIGURE 5-12. EFFECT OF MATERIAL PROPERTIES AND IMPULSE ON ATTENUATION RATE

Further support for the hypothesis that the speed of unloading waves dominates attenuation rates comes from comparing the attenuation rates in Cases 2, 3, and 5 with that in Case 4. This represents a correlation between unloading wave speeds and attenuation rates. There is no such simple correlation between amount of energy initially in the wave and attenuation rate, as comparison among Cases 2, 4, and 5 shows.

The most dramatic illustration of the effect of volumetric properties on attenuation rate is given by Case 4, which differs from Case 5 only in having plastic dilatation. At  $r/r_0 = 4$ ,  $\sigma_r$  in Case 4 is twice as great as that in Case 5.

## EFFECT OF PULSE SHAPE ON WAVE PROPERTIES

To test the hypothesis that the rates of attenuation depend heavily on the unloading waves catching up with the peak and to widen the scope of the study in general, two calculations were performed using input pulses of longer duration. The input pulse used in Cases 6 and 7 is illustrated in Figure 5-1b. The peak stress on the cavity wall is the same as in Cases 1 through 5, but the peak has a duration of  $7 \times 10^6$  sec. The shape of the unloading pulse is similar to Cases 1 through 5, and the impulse is about two times greater. The material properties assumed in Case 6 are the same as those in Case 4 while those in Case 7 are the same as those in Case 2.

The stress/time histories in Figure 5-5 and the rate of attenuation plot, Figure 5-13, confirm that lengthening the duration of the peak delays degradation of the pulse. Interpretation of Case 7 is difficult because the peak is associated with a very sharp rise and decay, which is the least favorable wave shape for the present method of calculation. Comparison of Case 2 with Case 7 suggests that the unloading wave catches up with the peak at about  $r/r_0 = 3-4$  in Case 7 and  $r/r_0 = 1-2$  in Case 2. This is confirmed by considering the instant in time at which the unloading wave catches up with the front of the loading wave. The maximum speed of unloading waves is

$$\sqrt{\frac{B_u + \frac{4G}{3}}{\rho}} = 1.94 \times 10^5 \text{ in./sec}$$



Unloading is initiated at  $r/r_0 = 1$  at  $t = 7.67 \times 10^{-6}$  sec. This signal arrives at  $r/r_0 = 4$  at  $t = 7.67 \times 10^{-6}$  sec +  $3 \ln./1.94 \times 10^5 \ln./\text{sec} = 23.2 \times 10^{-6}$  sec which approximately corresponds to the time of arrival of the front at the same station. In contrast, in Case 2 the unloading wave overtakes the peak almost immediately.

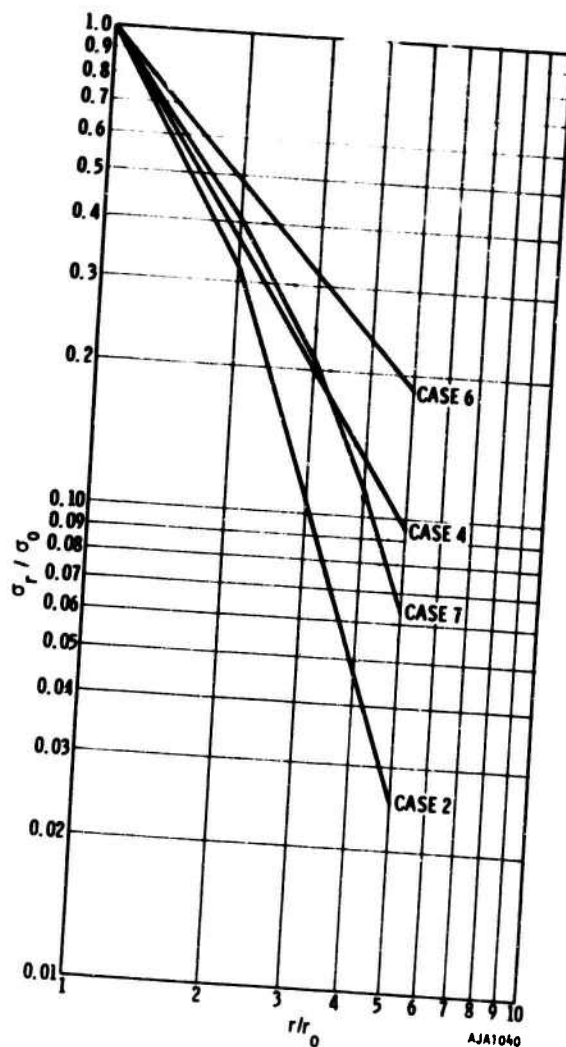


FIGURE 5-13. EFFECT OF MATERIAL PROPERTIES AND IMPULSE ON ATTENUATION RATE

AJA

R-6813-777

## SECTION 6

## IMPLICATIONS FOR MATERIAL PROPERTY TESTING

A mathematical model transforms experimental data from the states of stress under which the data were measured to states which occur in calculations. Since these states may differ widely, great reliance must be placed on the mathematical model to do the transformation correctly. Much of the doubt as to the physical meaning of calculations is due to uncertainty about the ability of current models to do this.

The risk involved in using a mathematical model in the present calculations could be lessened by basing the form of the model and the specific material property coefficients on laboratory experiments in which the states of stress are close to those encountered in the calculation. One use of the present calculations is to guide the planning of laboratory experiments on plane or cylindrical samples which support spherical wave field tests. The present calculations indicate the following two important areas of concentration.

- a.  $P/\mu$  relation for hydrostatic loading and unloading to indicate how the amount of hysteresis varies with  $\mu_{\max}$ .
- b. Stress/strain relations for loading programs in which the yield criterion and inelastic deformation investigated on unloading. See Figure 6-1.

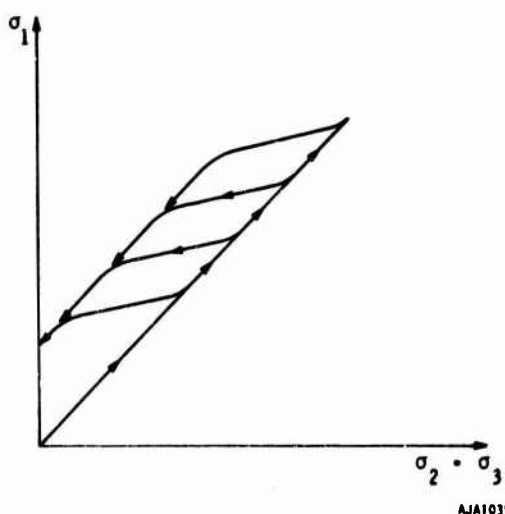


FIGURE 6-1. PROPOSED LOADING PROGRAMS FOR INVESTIGATING YIELD CRITERIA AND INELASTIC DEFORMATION ON UNLOADING

PRECEDING PAGE BLANK

The purpose of investigating the  $P/\mu$  relation under hydrostatic loading is to establish the amount of hysteresis in the absence of dilatancy, which is known to develop near the maximum deviatoric stress. Having established this, the amount of dilatancy which occurs during inelastic deformation on unloading may be investigated. The results will shed light on which of the two flow rules investigated in the present study is the more appropriate, and whether the yield criterion is the same on unloading as on loading.

These suggestions are intended to improve the effectiveness of the type of mathematical model used in the present calculation. It is possible that such experiments would expose the present model as being inadequate or misleading for application to spherical wave situation. In this event, it would become necessary to investigate new types of models.

SECTION 7  
CONCLUSIONS

The features of the present mathematical model which most strongly affect the results are

- a. The amount of permanent volumetric compaction during hydrostatic loading and unloading,
- b. The amount of dilatancy accompanying inelastic deformation,
- c. The yield criterion during unloading.

Laboratory testing should be concentrated in these areas to support the development of a model for use in spherical wave calculation.

AJA

R-6813-777

## REFERENCES

1. McKay, M. W., and C. S. Godfrey, *Study of Spherically Diverging Waves in Earth Media*, DASA-2223, Defense Atomic Support Agency, March 1969.
2. Clough, R. W., "The Finite Element Method in Structural Mechanics," *Stress Analysis*, Chapter 7, John Wiley and Sons, Ltd., 1965.
3. Wilson, E. L., *A Computer Program for the Dynamic Stress Analysis of Underground Structures*, University of California, January 1968.
4. Zienkiewicz, O. C., *The Finite Element Method in Structural and Continuum Mechanics*, McGraw-Hill, 1967.
5. Felippa, C. A., *Refined Finite Element Analysis of Linear and Nonlinear Two-Dimensional Structures*, SEL Report 66-22, University of California, 1966.
6. Hill, R., *The Mathematical Theory of Plasticity*, Clarendon Press, 1950.
7. Drucker, D. C., and W. Prager, "Soil Mechanics and Plastic Analysis or Limit Design," *Applied Mathematics*, Vol. X, No. 2, July 1952, pp. 57-165.
8. Prager, W., *An Introduction to Plasticity*, Addison-Wesley Publishing Company, 1959.
9. La Mori, P. N., *Compressibility of Three Rocks, (A) Westerly Granite and Solenhofen Limestone to 40 K Bar and 300 C, (B) Cedar City Tonalite to 40 K Bar at Room Temperature*, DASA-2151, Defense Atomic Support Agency, August 1968.
10. Saucier, K. L., *Properties of Cedar City Tonalite*, MP C-69-9, U. S. Army Corps of Engineers, Waterways Experiment Station, June 1969.
11. Petersen, C. F., *Shock Wave Studies of Selected Rocks*, Stanford Research Institute, May 1969.
12. U. S. Army Corps of Engineers, Missouri River Division Laboratory, *Strengthening of Rock Against Shock Effects, Tests for Strength Characteristics of Rock, Pile Driver Project*, MRD Report 64/90, September 1964.

PRECEDING PAGE BLANK

## REFERENCES (CONTINUED)

13. Brace, W. F., et al., "Dilatency in the Fracture of Crystalline Rocks," *Journal of Geophysical Research*, Vol. 71, No. 16, August 15, 1966, pp. 3939-3953.
14. Jones, A. H., and N. H. Froula, *Uniaxial Strain Behavior of Four Geological Materials to 50 Kilobars*, DASA-2209, Defense Atomic Support Agency, March 1969.
15. Schuster, S. H. and J. Isenberg, "Equations of State for Geologic Media," Vol. 2 *Free Field Ground Motion for Beneficial Siting*, ATI-AJA for SAMSO under Contract No. F04701-68-C-0192, October 24, 1969.
16. Hopkins, H. G., "Dynamic Expansion of Spherical Cavities in Metals," *Progress in Solid Mechanics*, Vol. 1, (I. N. Sneddon and R. Hill, Eds.), North-Holland Publishing Co., Amsterdam, 1964, Ch. III.
17. Jeffreys, H., *The Earth*, Cambridge University Press, 1962.
18. Kolsky, H., *Stress Waves in Solids*, Dover Publications, Inc., 1963.



## APPENDIX

An investigation was made of the effect of rise time on the pulse shape and attenuation rate of spherically diverging waves. The purpose of the study was to determine whether the rise time of the prescribed stress or velocity boundary condition significantly affects the calculated stress pulse at ranges between 1 and 5 times the cavity radius. For the rise times and material properties of interest to the present finite element calculations, the study indicates that the true rise time should be represented as accurately as possible. The initial rise time of about  $0.67 \times 10^{-6}$  sec, which was measured in the Physics International Company experiments, was chosen as being representative of shock waves generated by detonating chemical explosive. The finite element mesh size and integration time step were selected so as to represent this initial rise time as accurately as possible.

In the first part of the study, use was made of Jeffreys' solution (Reference 17) for a step pressure pulse on the wall of a cavity whose radius is  $r_0$ . The particle velocity at a range  $r$  is given by the following expression:

$$\dot{u} = \frac{i}{6} \frac{r_0 \sigma_0 c_p}{G r^2} \left[ r_0 \sqrt{2} - \sqrt{2} \left( r - \frac{r_0}{2} \right) \sin \sqrt{2} \beta + 2r \cos \sqrt{2} \beta \right] \exp(-\beta) \quad (A-1)$$

where  $\dot{u}$  = Radial particle velocity

$r_0$  = Cavity radius

$r$  = Range

$\sigma_0$  = Applied radial stress on the cavity wall

$c_p$  = Dilatational wave speed

$G$  = Shear modulus

The solution applies subject to the restriction that

$$\beta = \frac{c_p t - (r - r_0)}{r_0} \geq 0$$

Although this solution applies to the case of a step load in a cavity, it can be used to obtain an estimate of the solution for a ramp load by summing up the effects of many small step loads, as illustrated in Figure A-1. Several cases were studied using Jeffreys' solution. One of these was compared with the corresponding finite element solution.

Case	Solution Method	$\frac{t_p}{\tau_p}$
A1	Jeffreys	0.
A2	Jeffreys Adapted	0.0055 sec
A3	Finite Element	0.0055 sec

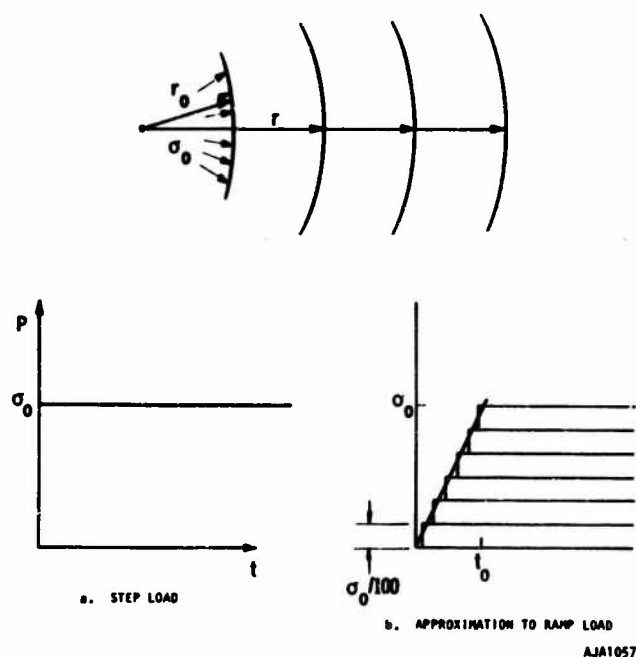


FIGURE A-1. INPUT FOR JEFFREYS' SOLUTION

The following geometrical, material, and loading parameters are common to all three cases.

$$c_p = 1.465 \times 10^5 \text{ in./sec}$$

$$G = 2.013 \times 10^6 \text{ psi}$$

$$r_o = 100 \text{ in.}$$

$$\sigma_o = 0.04775 \text{ psi}$$

The velocity time history for each case is obtained at  $r/r_o = 2.44$ . The results which are plotted in Figure A-2 are typical of the dramatic effect of rise time on the peak particle velocity and pulse shape.

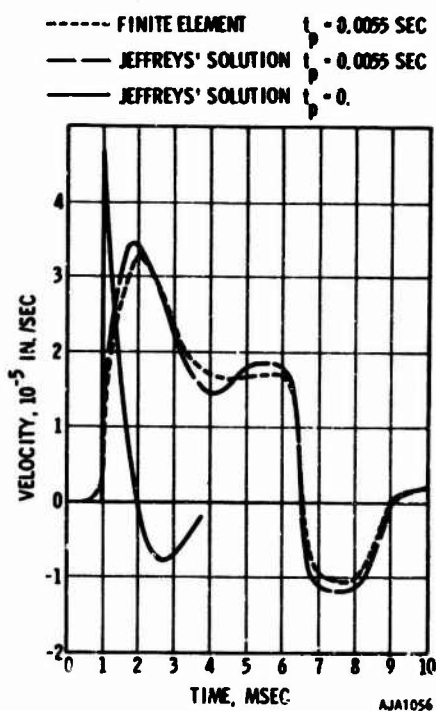
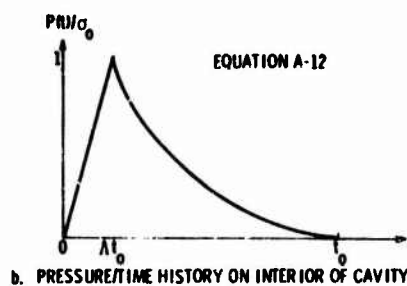
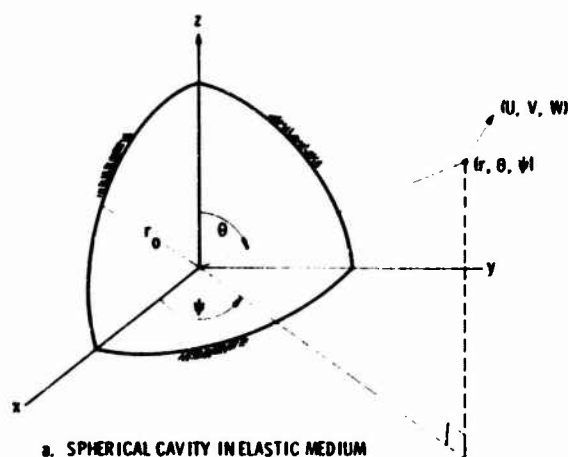


FIGURE A-2. VELOCITY/TIME HISTORY AT  $r/r_o = 2.44$

A second study was initiated to study the effect of rise time on the shape and attenuation rate of a wave having the same initial shape as the one used in the present finite element calculations. This shape is represented in the analysis by a linear rise to a peak pressure followed by an exponential decay. Figure A-3 illustrates the shape of the input pulse and the geometrical coordinates of the analysis.



AJA1055

FIGURE A-3. COORDINATES AND PRESSURE/TIME HISTORY FOR RAMP LOAD WITH EXPONENTIAL DECAY

Consider the configuration shown in Figure A-3. A spherical cavity of radius  $r_0$  in an infinite body initially at rest is subjected to an internal pressure  $p(t)$  at the boundary  $r = r_0$ . Under the assumed condition of spherical symmetry and infinitesimal displacements, the response at a point P at an arbitrary position  $(r, \theta, \psi)$  is to be determined. Due to spherical symmetry, the components of displacement in the  $\theta$  and  $\psi$  directions,  $v$  and  $w$ , respectively, vanish. The remaining response parameters are functions of  $r$  and  $t$  only. Since only infinitesimal displacements are considered, no distinction need be made between deformed and undeformed positions.

The only nontrivial equation of motion is that in the radial direction (for a general theory of elastic wave propagation; see Kolsky, Reference 18) and when expressed in terms of the dilatational displacement potential function  $\psi$  it becomes simply the one-dimensional spherical wave equation

$$\nabla^2 \psi \equiv \frac{\partial^2 \psi}{\partial r^2} + \frac{2}{r} \frac{\partial \psi}{\partial r} = \frac{1}{c_p^2} \frac{\partial^2 \psi}{\partial t^2} \quad (\text{A-2})$$

$$\text{where } \psi = \psi(r, t) \quad \begin{cases} r_0 < r < \infty \\ 0 < t < \infty \end{cases}$$

and  $c_p = \sqrt{(\lambda + 2\mu)/\rho}$  is the dilatational wave speed and  $\lambda, \mu$  are the Lamé constants. The dilatation potential  $\psi$  is related to the radial displacement  $u$  by

$$u = \frac{\partial \psi}{\partial r} \quad (\text{A-3})$$

The radial stress  $\sigma_r$  and tangential stresses  $\sigma_\theta, \sigma_\psi$  are obtained from

$$\sigma_r = (\lambda + 2\mu) \frac{\partial u}{\partial r} + 2\lambda \frac{u}{r} = (\lambda + 2\mu) \frac{\partial^2 \psi}{\partial r^2} + \frac{2\lambda}{r} \frac{\partial \psi}{\partial r} \quad (A-4)$$

$$\sigma_\theta = \sigma_\psi = 2(\lambda + \mu) \frac{u}{r} + \lambda \frac{\partial u}{\partial r} = \frac{2(\lambda + \mu)}{r} \frac{\partial \psi}{\partial r} + \lambda \frac{\partial^2 \psi}{\partial r^2}$$

All shear stresses are zero as a result of symmetry.

At the boundary  $r = r_0$ ,

$$\sigma_r = -P(t)$$

or

$$\left[ (\lambda + 2\mu) \frac{\partial^2 \psi}{\partial r^2} + \frac{2\lambda}{r} \frac{\partial \psi}{\partial r} \right]_{r=r_0} = -P(t) \quad (A-5)$$

and with  $r \rightarrow \infty$ ,  $\psi$  is taken to be zero since the medium far enough away from the cavity is undisturbed for finite times.

The Laplace transform of  $\psi(r, t)$  is denoted by

$$\bar{\psi}(r, p) = \int_0^\infty e^{-pt} \psi(r, t) dt$$

Applying this operation to the differential equation (A-2) provides

$$\frac{d^2 \bar{\psi}}{dr^2} + \frac{2}{r} \frac{d\bar{\psi}}{dr} - k_d^2 \bar{\psi} = 0 \quad (A-6)$$

where  $k_p = p/c_p$ . The solution to Equation A-6 is, accordingly,

$$\bar{\psi}(r,p) = \frac{A(p)}{r} e^{-k_p r} + \frac{B(p)}{r} e^{+k_p r}$$

where  $A(p)$ ,  $B(p)$  are arbitrary functions of  $p$ . The boundary condition at  $r \rightarrow \infty$  suggests taking  $B(p) = 0$  so that

$$\bar{\psi}(r,p) = \frac{A(p)}{r} e^{-k_p r} \quad (A-7)$$

Application of the Laplace transform to Equation A-5 yields

$$(\lambda + 2\mu) \frac{d^2 \bar{\psi}}{dr^2} + \frac{2\lambda}{r} \frac{d\bar{\psi}}{dr} = -\bar{P}(p) \quad (A-8)$$

where  $\bar{P}(p)$  is the Laplace transform of  $P(t)$ . Equations A-7 and A-8 together determine the arbitrary function  $A(p)$  and it is found that

$$\bar{\psi}(r,p) = -\frac{r_0}{\rho r} \frac{\bar{P}(p) e^{-p(r-r_0)/c_p}}{(p+p_1)(p+p_2)} \quad (A-9)$$

where  $p_1 = 2\alpha(1 + i\beta)$

$p_2 = 2\alpha(1 - i\beta)$

$\alpha = c_s^2 / r_0 c_p$

$\beta = \sqrt{(c_p/c_s)^2 - 1}$

and  $c_s = \sqrt{\mu/\rho}$  is the shear wave speed. A formal solution to the problem is therefore given by the inverse Laplace transform of Equation A-9:

$$\psi(r,t) = -\frac{r_0}{2\pi i \rho r} \int_C \frac{\bar{P}(p) e^{p[t - (r-r_0)/c_p]}}{(p+p_1)(p+p_2)} dp \quad (A-10)$$

# AJA

R-6813-777

where  $C$  denotes a suitable contour in the complex  $p$ -plane. Equation A-9 can also be written as

$$\bar{\psi}(r,p) = \frac{r_0}{pr} \frac{\bar{P}(p)}{p_2 - p_1} \left[ \frac{1}{p + p_1} - \frac{1}{p + p_2} \right] e^{-p(r - r_0)/c_p} \quad (A-11)$$

which is a more convenient form for the inversion process.

Consider the exponential pulse given by

$$\begin{aligned} \frac{P(t)}{\sigma_0} &= \frac{t}{\Lambda t_0} [H(t) - H(t - \Lambda t_0)] \\ &+ \frac{1 - t/t_0}{1 - \Lambda} \sum_{n=1}^N a_n e^{-b_n(t - \Lambda t_0)/t_0} [H(t - \Lambda t_0) - H(t - t_0)] \end{aligned} \quad (A-12)$$

where  $H(t)$  is the Heaviside step function

$$H(t) = \begin{cases} 0 & \text{if } t < 0 \\ 1 & \text{if } t > 0 \end{cases}$$

and  $N$  is any integer. The pressure pulse given by Equation A-12 is called an  $N$ -term exponential pressure pulse. It can be shown that the Laplace transform of Equation A-12 is

$$\begin{aligned} \frac{\bar{P}(p)}{\sigma_0} &= \frac{1}{\Lambda t_0 p^2} - \left[ \frac{1}{p} + \frac{1}{\Lambda t_0 p^2} \right] e^{-\Lambda t_0 p} \\ &+ \sum_{n=1}^N a_n \left[ \frac{1}{p + b_n/t_0} - \frac{1}{(1 - \Lambda) t_0 (p + b_n/t_0)^2} \right] e^{-\Lambda t_0 p} \\ &+ \frac{1}{(1 - \Lambda) t_0} \sum_{n=1}^N a_n \frac{e^{-b_n(1 - \Lambda)}}{(p + b_n/t_0)^2} e^{-t_0 p} \end{aligned} \quad (A-13)$$



# AJA

R-6813-777

Substituting Equation A-13 into Equation A-11 and carrying out the inversion operation leads finally to

$$\begin{aligned}
 \psi(r,t) = & \frac{a\sigma_o}{2\alpha\beta\rho r} \operatorname{Im} \left[ \frac{1}{\Lambda t_o p_1^2} \left\{ \left[ e^{-p_1 \tau} + p_1 \tau - 1 \right] H(\tau) - \left[ e^{-p_1 (\tau - \Lambda t_o)} \right. \right. \right. \\
 & \left. \left. + p_1 (\tau - \Lambda t_o) - 1 \right] H(\tau - \Lambda t_o) \right\} + \frac{1}{p_1} \left\{ e^{-p_1 (\tau - \Lambda t_o)} - 1 \right. \\
 & \left. + p_1 \sum_{n=1}^N \frac{a_n}{p_1 - b_n/t_o} \left[ e^{-b_n (\tau - \Lambda t_o)/t_o} - e^{-p_1 (\tau - \Lambda t_o)} \right] \right\} H(\tau - \Lambda t_o) \\
 & - \frac{1}{(1 - \Lambda) t_o} \left\{ \sum_{n=1}^N \frac{a_n}{(p_1 - b_n/t_o)^2} \left[ e^{-p_1 (\tau - \Lambda t_o)} \right. \right. \\
 & \left. \left. + (p_1 - b_n/t_o) (\tau - \Lambda t_o) e^{-b_n (\tau - \Lambda t_o)/t_o} - e^{-b_n (\tau - \Lambda t_o)/t_o} \right] H(\tau - \Lambda t_o) \right. \\
 & - \sum_{n=1}^N \frac{a_n e^{-b_n (1 - \Lambda)}}{(p_1 - b_n/t_o)^2} \left[ e^{-p_1 (\tau - t_o)} + (p_1 - b_n/t_o) (\tau - t_o) e^{-b_n (\tau - t_o)/t_o} \right. \\
 & \left. \left. - e^{-b_n (\tau - t_o)/t_o} \right] H(\tau - t_o) \right\} \Bigg] \quad (A-14)
 \end{aligned}$$

where  $\tau = t - (r - r_o)/c_p$

$$p_1 = 2\alpha(1 + i\beta)$$

$$\alpha = c_s^2 / r_o c_p$$

$$\beta = \sqrt{(c_p/c_s)^2 - 1}$$

and  $\operatorname{Im}$  denotes the imaginary part of a complex function.

Expressions for  $u$ ,  $\sigma_r$ , and  $\sigma_\theta$  can be obtained from Equations A-3, A-4, and A-14. The radial velocity  $\dot{u}$  is obtained by differentiating  $u$  with respect to time (the lengthy algebra involved will not be reproduced here). Note that the radial displacement  $u$  has terms of the form  $(r_0/r)$  and  $(r_0/r)^2$ , while the radial velocity  $\dot{u}$ , the radial stress  $\sigma_r$ , and the tangential stress  $\sigma_\theta$  have in addition terms of the form  $(r_0/r)^3$ . The response has the general character of a highly damped oscillatory motion about the static value. The damping time constant  $T$  is given by

$$\frac{1}{T} = 2\alpha\beta$$

$$\text{where } \alpha = \frac{c_s/r_0}{c_p/c_s}$$

$$\beta = \sqrt{(c_p/c_s)^2 - 1}$$

Hence,  $T$  is of the order of the half transit time  $t_T = a/c_s$ , i.e., the time for a shear disturbance to travel a distance equal to the radius of the cavity. Near the wave front, the stresses decay like  $(r_0/r)$  with increasing radial distances. Behind the front, the decay rate is somewhat higher depending on the value of the time after wave front arrival,  $\tau$ , compared to  $T$ . The limit, of course, is  $(r_0/r)^3$  for the static case. Therefore, the peak response depends not only on the peak input (as in all linear systems) but also on how soon the peak is attained. In other words, if the input pulse reaches its peak in a time smaller than the characteristic damping time  $T$ , the response peaks are expected to scale according to  $(r/r_0)^{-1}$ . If the input peak is not reached until after several multiples of  $T$ , however, the response peaks are expected to scale according to  $(r/r_0)^{-3}$ . This observation is verified by the results obtained for the specific examples considered below.

Numerical results are obtained for the exponential input pulses defined by the following parameters.

$$\begin{aligned} a_1 &= 0.65 \\ a_2 &= 0.35 \\ b_1 &= 10 \\ b_2 &= 0.1 \\ p_o &= -475,000 \text{ psi} \\ t_o &= 40 \times 10^{-6} \text{ sec} \end{aligned}$$

Case	$t_p = \Delta t_o$
B1	0.
B2	$0.6667 \times 10^{-6} \text{ sec}$
B3	$2.0 \times 10^{-6} \text{ sec}$
B4	$5.0 \times 10^{-6} \text{ sec}$

These parameters describe pressure time histories on the surface of the cavity which cover the range observed in the present finite element calculations. Although the input pulse in all the finite element calculations has an initial rise time of  $0.6667 \times 10^{-6} \text{ sec}$  (Case B2), the rise time lengthens to  $2.0 \times 10^{-6}$  to  $3.0 \times 10^{-6}$  at  $r/r_o = 4$  to 5. This lengthening is due to numerical distortion of the pulse which evidently cannot be entirely eliminated in spite of using small mesh size and integration time step. Thus, Cases B1 through B4 bound the possible effects on pulse shape and attenuation rate which can be attributed to rise time in the present elastic finite element calculations.

The medium surrounding the cavity has the same properties as the medium in Case 1 of the finite element calculations. These are

$$\begin{aligned} B &= B_o = 1.205 \times 10^6 \text{ psi} \\ G &= 1.000 \times 10^6 \text{ psi} \\ \rho &= 0.000238 \text{ lb-sec}^2/\text{in.}^4 \end{aligned}$$

The p- and s-wave speeds in the material are

$$c_p = 8590 \text{ ft/sec}$$

$$c_s = 5400 \text{ ft/sec}$$

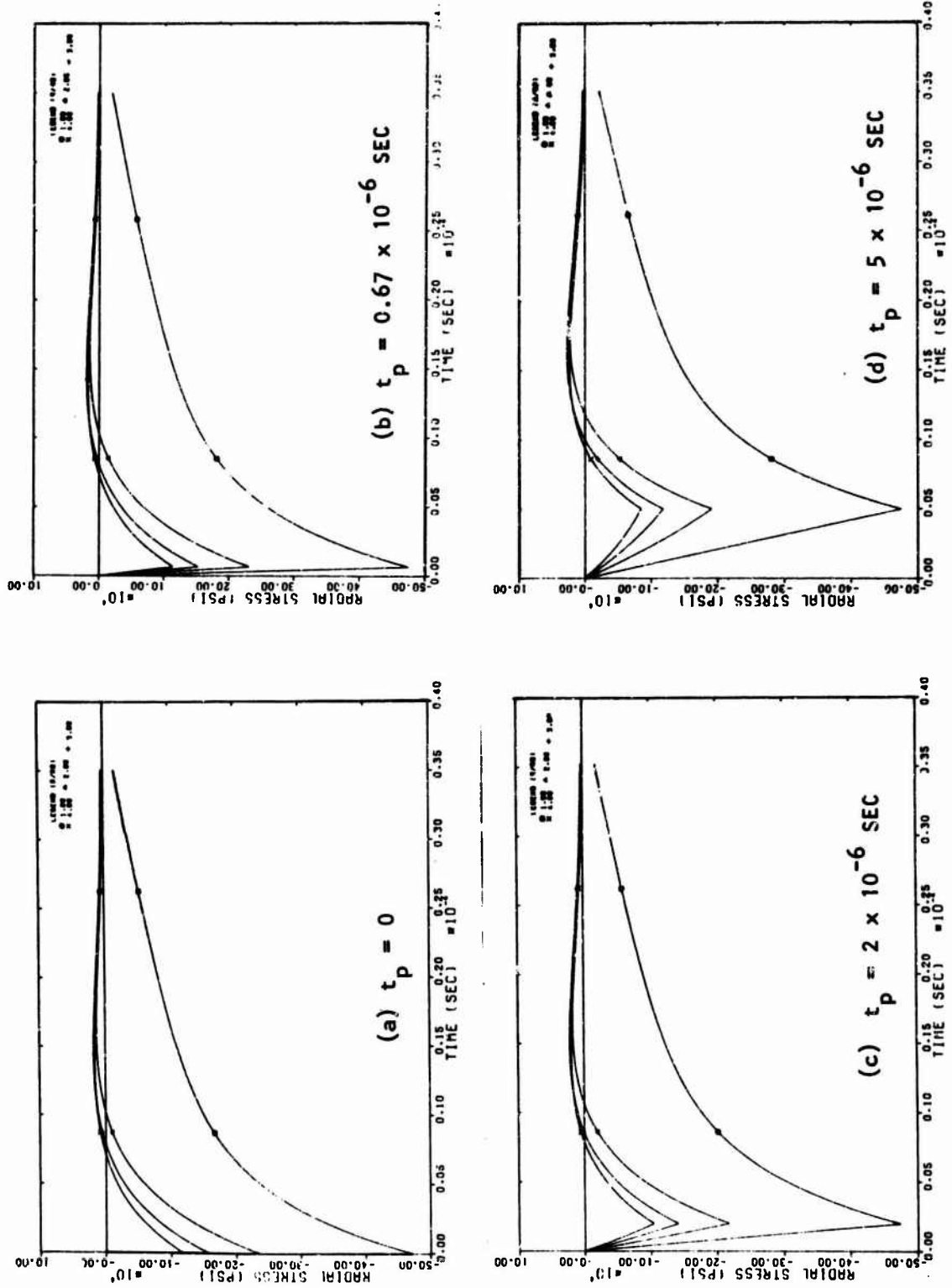
The cavity is assumed to have an initial radius  $r_0 = 1$  in.

The responses in the four cases are shown at  $r/r_0 = 1, 2, 3,$  and  $4$  in Figures A-4 and A-5. The computer program which was used to calculate the response automatically defines the arrival time at each station to be zero. Hence, the response at all four ranges of a given case appear to start at zero, whereas in a physical problem each would have different times of arrival.

Except in Case B4, when the portion of the  $\sigma_r/t$  history prior to the peak is slightly nonlinear, there is no noticeable distortion of the pulse due to the various rise time studied. The rates of attenuation, which are shown in Figure A-6, differ appreciably due to the different rise times. For example, at  $r/r_0 = 4$ ,  $\sigma_r/\sigma_0$  in Case B1 is 1.45 times that in Case B4. This effect is considered to be too big to be ignored, and hence, care was used in representing rise times in the finite element calculations.

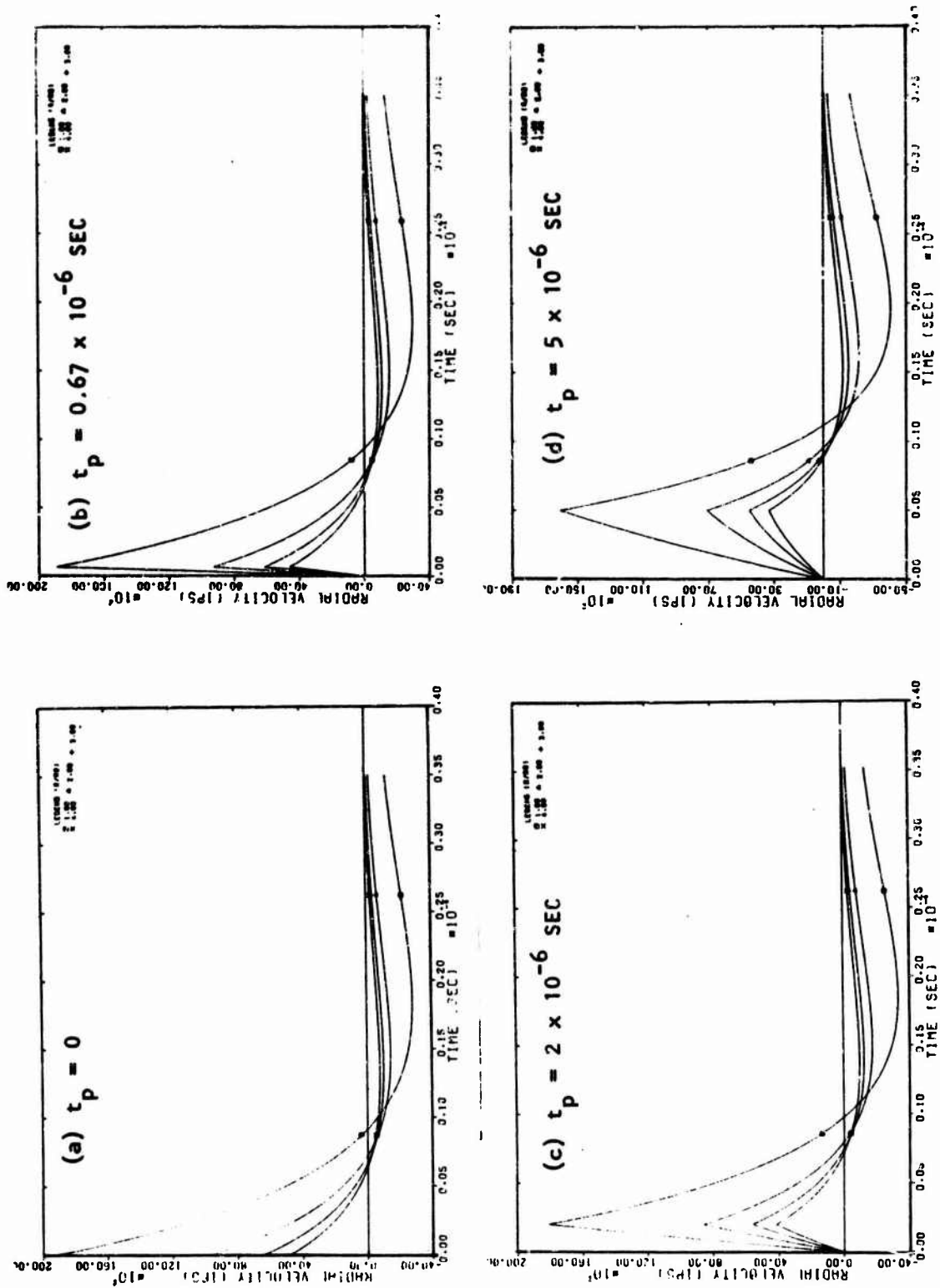
An estimate of the numerical error present in the finite element calculations is indicated by comparing the attenuation rate found in Case 1 with the rates of attenuation found in the closed form solutions.

The formal integral solution is obtained for spherical waves propagating from a spherical cavity subjected to a pressure pulse with finite rise time and exponential decay. The rate of attenuation of the peak stress when it propagates into the medium depends on the magnitude of the rise time relative to the transit time  $r_0/c_s$ , where  $r_0$  is the radius of the cavity and  $c_s$  is the shear wave speed. For zero rise time, the attenuation rate is proportional to  $r^{-1}$ , whereas for rise times much greater than  $r_0/c_s$  the attenuation rate is proportional to  $r^{-3}$ .



AJA1038

FIGURE A-4. RADIAL-STRESS/TIME HISTORIES FOR VARIOUS RISE TIMES



AJA1037

FIGURE A-5. RADIAL-VELOCITY/TIME HISTORIES FOR VARIOUS RISE TIMES

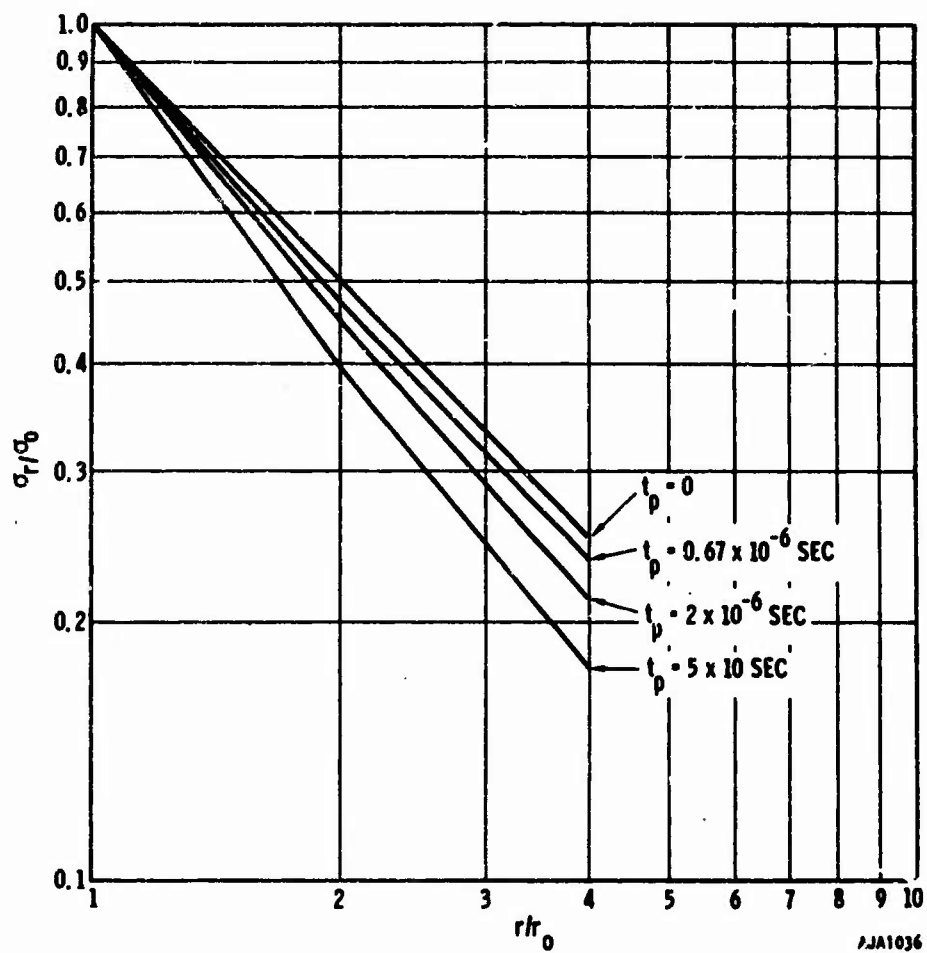


FIGURE A-6. EFFECT OF RISE TIME ON ATTENUATION RATE

UNCLASSIFIED  
Security Classification

DOCUMENT CONTROL DATA - R & D		
(Security classification of title, body of abstract and indexing annotation must be entered when the overall report is classified)		
1. ORIGINATING ACTIVITY (Corporate author)		2a. REPORT SECURITY CLASSIFICATION
Agbabian-Jacobsen Associates		UNCLASSIFIED
		2b. GROUP
3. REPORT TITLE		
Spherical Waves in Inelastic Materials		
4. DESCRIPTIVE NOTES (Type of report and inclusive dates)		
5. AUTHOR(S) (First name, middle initial, last name)		
J. Isenberg A. K. Bhaumik F. S. Wong		
6. REPORT DATE	7a. TOTAL NO. OF PAGES	7b. NO. OF REFS
October 1964		
8a. CONTRACT OR GRANT NO.	9a. ORIGINATOR'S REPORT NUMBER(S)	
DASA-01-68-C-0081	AJA-R-6813-777	
b. PROJECT NO.	9b. OTHER REPORT NO(S) (Any other numbers that may be assigned this report)	
c. SB 047	DASA 2404	
d.		
10. DISTRIBUTION STATEMENT		
This document has been approved for public release and sale; its distribution is unlimited.		
11. SUPPLEMENTARY NOTES		12. SPONSORING MILITARY ACTIVITY
		Director Defense Atomic Support Agency Washington, D. C. 20305
13. ABSTRACT		
<p>The effects of constitutive properties on spherical wave propagation are investigated through finite element calculations of an infinite medium (Cedar City Tonalite) loaded internally by a sphere of chemical explosive. Detonation of the explosive is represented by applying a pressure to the cavity surface which varies with time in a manner similar to that measured experimentally by Physics International Company.</p> <p>Results are presented as stress/time histories and stress strain relations at various cavity radii and as rates of attenuation of the peak radial stress. The results illustrate the effect of varying the bulk modulus, yield criterion and plastic flow rule.</p>		

DD FORM 1473 (PAGE 1)  
NOV 63  
0102-014-6600

UNCLASSIFIED  
Security Classification



UNCLASSIFIED

Security Classification

14 KEY WORDS	LINK A		LINK B		LINK C	
	ROLE	WT	ROLE	WT	ROLE	WT
Constitutive Relations Spherical Wave Propagation						

DD FORM 1 NOV 65 1473 (BACK)  
(PAGE 2)

UNCLASSIFIED  
Security Classification